

---

## Pore Pressure, Compaction and Tectonics

### 2.1 Introduction

Most physical transport and related processes depend on both, temperature and pressure. Pressure is one of the fundamental physical values. It is a scalar, which is represented with a single value in each location. The term pressure has only a real meaning for fluids and not solids. In porous media, pressure is often introduced as the pressure within the fluids in the pores, the pore pressure. The equivalent physical entity in solids is the stress tensor, which is a symmetrical  $3 \times 3$  tensor with six independent values (Sec. 8.2). It can be illustrated with an ellipsoid, whose axes represent the principal stresses in size and direction. Usually, only single components or invariants of the stress tensor are important. Both, rock stress and pore pressure describe the response of the material to an external load. The “average” stress of the porous volume element is called bulk stress. It is therefore a superposition or mixture of pore pressure and rock stress and it has to be in equilibrium with all external loads.

The primary pressure and stress causing process is sedimentation with subsidence, which produces overburden load on the subsurface rocks. Stresses and pore pressures generally increase with depth. Rock stresses and fluid pressures interact with compaction and porosity reduction. The main mechanisms for compaction are rearrangement of the grains to denser packages and cementation, which are called mechanical and chemical compaction, respectively. In summary, three main ingredients needed to formulate a model for the mechanics of the porous sediments, are the concepts of bulk stress, pore pressure and compaction. Additional effects, like mineral transformation, aquathermal pressuring, and kerogen cracking or fracturing, should also taken into account.

#### 2.1.1 Bulk Stresses

A homogeneous body under a constant load from above deforms horizontally and vertically as shown in Fig. 2.1.a. The vertical stress in each location is

then equal to the top load and the horizontal stress is equal to zero. This stress state is called uniaxial. If the side boundaries of the bodies are fixed (Fig. 2.1.b), the horizontal stress components are compressive as well and equal to a fixed ratio of the top load, namely  $\sigma_h/\sigma_v = \nu/(1 - \nu)$ . The Poisson ratio  $\nu$  is a material constant and sediments have numbers of 0.1 ... 0.4, which yield stress ratios of 0.11 ... 0.67. Exceptions are salt and unconsolidated sands with Poisson ratios close to 0.5.

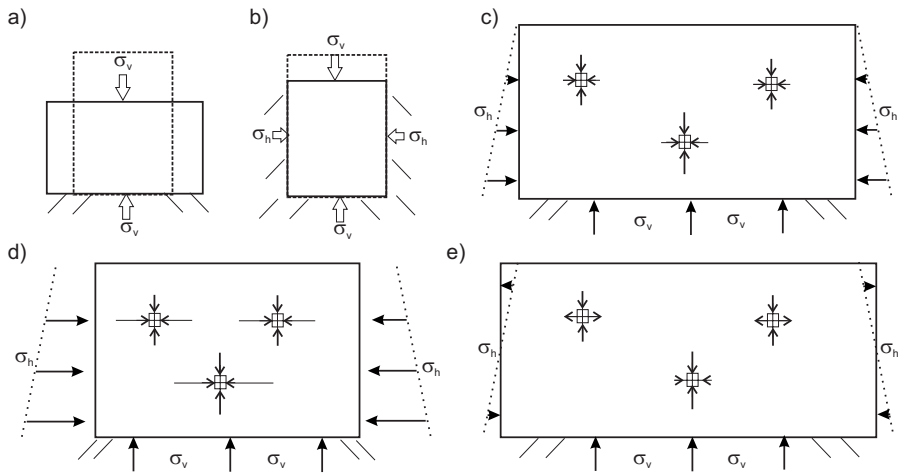


**Fig. 2.1.** Vertical and horizontal stresses in a homogeneous solid with overburden (a) load on top with free moving sides; (b) load on top with fixed side boundaries (c) gravity loads with fixed side boundaries; (d) together with additional constant compressions on the side boundaries; (e) together with additional constant tensions on the side boundaries

The situation in non-tectonically influenced basins is similar to the fixed solid case (Fig. 2.1.c) with vertical loads increasing approximately linearly with depth. Heterogeneities of geomechanical properties cause different stress ratios and rotation of the main stress axes. Fault planes and salt domes disturb homogeneous trends in stress. Tectonic processes generally add a compressive or tensile stress to the horizontal component (Fig. 2.1.d,e). Extensions of the model to lower horizontal stresses can revert the compressive (positive) stresses into tensile (negative) stresses, while compressive boundaries can increase the horizontal stresses so that they exceed the vertical stresses and become the maximum principal stress.

The stress state in solid grains is mainly controlled by the overburden load of the considered volume element in the case of negligible tectonic forces and homogeneously layered rocks (Fig. 2.1.c). Then, the "lithostatic pressure" approach can be used, which describes the three dimensional stress field by one single value, the lithostatic pressure, assuming the following simplifications:

- The three main stress axes are straight vertically and horizontally directed. This assumption is not valid in heterogeneous layers and salt domes, where the coordinate system of the principal stress components rotates.
- The boundaries of the basins are fixed in terms of displacements, the horizontal stresses are equal in both directions and the stress ratio ( $\sigma_h/\sigma_v$ ) is constant. The elastic properties are isotropic and layerwise homogeneous. It also means that the model has no tectonic stresses due to compressional or extensional forces or displacements.
- The vertical stress component is equal to the overburden load. This means that all stresses are conducted straight vertically and will not influence each other.

The vertical component is then equal to the overburden weight, the lithostatic pressure. It represents the 'pressure' state of the porous bulk element.

### 2.1.2 Pore Pressure Formation and Fluid Flow

The measurable pressure value in the pore fluid is the pore pressure. It is mainly caused by the overburden weight, but fluid flow together with compaction can decrease the overburden induced pressure and the resulting pore pressure is usually smaller than the lithostatic pressure. In a non-compactable porous rock, the lithostatic pressure and the pore pressure are both equal to the overburden load. Fluid outflow allows grain rotation to more compact packages, which decreases pore pressure and porosity. Thus, the difference between lithostatic and pore pressure is a measure of compaction.

Ideal compaction does not reduce pore pressure to zero. Instead a hydrostatic pressure remains, which is equal to the weight of the overlaying water column. Generally, the hydrostatic pressure is defined as the part of the pore pressure which does not contribute to water flow. The hydrostatic zero level can be arbitrarily defined, since only gradients and not absolute values of pressures control pore water flow. The groundwater table is not suitable as a constant reference level, since it varies over basin scale. Instead, the seawater level is used as the hydrostatic zero level. The hydrostatic pressure is then equivalent to the water column weight measured from the seawater level and therefore depends on sea and pore water density. Note that the hydrostatic pressure is not a measurable pressure. It is a theoretical pressure for ideal compactable layers or slow sedimentation.

The difference between the pore pressure and the hydrostatic pressure is the overpressure which directly controls water flow (Fig. 2.2). The pore pressure lies usually between hydrostatic and lithostatic pressure, but there are exceptions. It can be lower than the hydrostatic pressure when high uplift and erosion rates act on deep sand layers which are connected to near surface pressure areas along permeable facies. It can also exceed lithostatic pressures when large overpressures are built up by gas generation or highly permeable facies are connected at large depth levels.

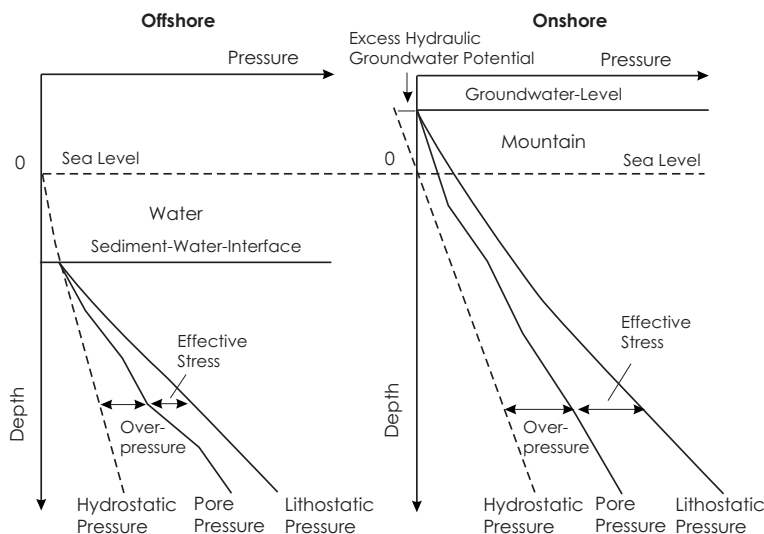


**Fig. 2.2.** Definitions of pressures and stresses. The groundwater level is often assumed to match the surface in basin modeling. Then, pore and lithostatic pressure have the same zero level, as shown here

One can distinguish between three processes of overpressure build up: overburden load together with mechanical under-compaction, cementation and overpressuring caused by fluid expansion processes (Osborne and Swarbrick, 1997; Swarbrick et al., 2002).

Overburden load induced pore pressure formation due to incomplete sediment compaction, as explained above, is the main process for overpressure formation. Here, compaction is the rearrangement of grains to denser packages with a reduction in pore space related to a decrease in pore throats and connectivity of the pore network. This process of grain rotation, crushing and deformation is called mechanical compaction. Compaction is caused by overburden load. The load acts on the pore fluid and the rock grains according to their compressibilities. Incremental fluid outflow generates a difference between rock stresses and pore pressure, which allows compaction. Compaction in turn changes the ratio between the rock stresses and the fluid pressure, since it decreases the rock and bulk compressibility, enforces further fluid outflow, and decreases the thickness of the solid matrix. The result of this coupled process is always a reduction of overpressure since the outflow from the compacting element is greater than the local increase of overpressure due to the thinning of the solid matrix. This is ensured as the compaction law is formulated in a manner, that relates porosity loss with effective stress increase. Finally, mechanical compaction is considered to be an overpressure reducing process (Fig. 2.3.a). The remaining overpressure could be simply in-

terpreted as a result of incomplete compaction and that is why this process of overpressure formation is called under-compaction.

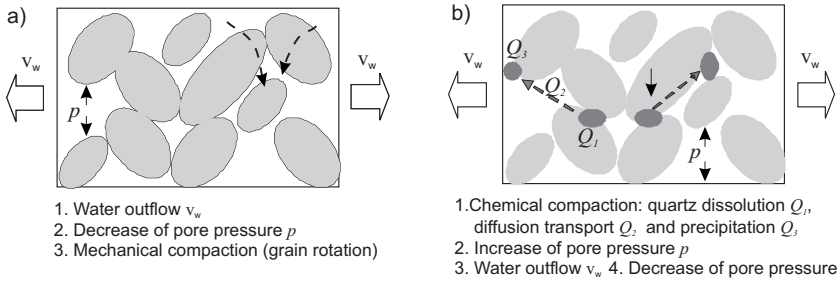


**Fig. 2.3.** Overpressure and Compaction: (a) mechanical compaction is a result of water outflow, it is always related to decrease in overpressure. (b) Quartz cementation and related compaction transfers lithostatic to pore pressure. It increases pore pressure. Water outflow can partially decrease the overpressure afterwards

Another source for overpressure is chemical compaction due to cementation. Cementation occurs in all sandstones and carbonates. It significantly decreases the porosity, and is mainly responsible for porosity reduction at large depths, where mechanical compaction is almost negligible. Cementation is the result of dissolution of quartz from the horizontal contact areas, diffusive transport within the pore water, and precipitation of a silican cement on free quartz surfaces. Quartz dissolution is mainly stress controlled. Temperature affects the diffusion constant and precipitation rate. Chemical compaction increases overpressure, since rock stress is transferred from the rock matrix to pore pressure. Cementation also drives fluid outflow and compaction with the generated overpressure as the main driving force (Fig. 2.3.b).

The third group of overpressure generating processes encompasses fluid expansion mechanisms: oil and gas generation, oil to gas cracking, aquathermal expansion and mineral changes such as smectite to illite conversion. In all these processes, mass or the density of the fluids changes and yields fluid pressure increase controlled by fluid compressibility. The overpressure increase due to fluid expansion mechanisms is usually small compared to those related to mechanical and chemical compaction.

### 2.1.3 Compaction and Porosity Reduction

Compaction is the reduction of the sediment bulk volume and is equivalent to volumetric strain  $\epsilon_v = V/V_0$ , the ratio of a load bearing volume  $V$  to the unloaded initial volume  $V_0$ . The average of the volumetric change of a specimen is called the mean stress  $\bar{\sigma}$ . Stresses and strains are further explained in the Sec. 2.6. A compaction law relates volumetric strain to mean stress changes with an elastic parameter.

	Rock Compaction	Pore Space Compaction
Elastic	Elasticity of the Grains	Elasticity of the Skeleton Elasticity of the Pore Fluid
Plastic	Plasticity of the Grains	Rearrangement of the Grains Pressure Dissolution

**Table 2.1.** Compaction related Mechanisms

$$C = -\frac{1}{V} \frac{\partial V}{\partial \bar{\sigma}} = \frac{\partial \epsilon_v}{\partial \bar{\sigma}}. \quad (2.1)$$

Compaction mainly decreases porosity, but also reduces the grain volume. Generally, the rock and pore volumes are reduced with reversible (elastic) and irreversible (plastic) contributions. Some of the special mechanisms acting on microscopic and mesoscopic scales are listed in Table 2.1 after Schneider et al. (1996).

The compressibility in equation (2.1) is mainly a property of the grain framework and is called bulk compressibility. In the absence of a pore fluid, it relates the bulk volume decrease with the mean total stress. The presence of a pore water retards compaction, which as a first approximation can be described as the introduction of a mean effective stress  $\bar{\sigma}' = \bar{\sigma} - p$  instead of the mean total stress in (2.1) with a reduction of the pore pressure  $p$ . Terzaghi (1923) confirmed this thesis experimentally, by proving that increasing the mean total stress or decreasing the pore pressure yields the same amount of compaction. Generally, Terzaghi's effective stress can also be introduced as a stress tensor  $\boldsymbol{\sigma}'$ .

$$\boldsymbol{\sigma}' = \boldsymbol{\sigma} - p \mathbf{I} \quad (2.2)$$

where  $\mathbf{I}$  is the unit tensor (Chap. 8).

In practice, compaction laws on the basis of Terzaghi's effective stress definition are written in terms of porosity loss versus the vertical component of the effective stress  $\sigma'_z$ . The usage of porosity change instead of the volumetric bulk strain neglects volume changes of the solid matrix which are small. The restriction to the vertical effective stress means that a fixed ratio between horizontal and vertical stresses is assumed. The corresponding vertical total stress can then be simply approximated by the overburden sediment load pressure  $p_l$ .

$$\frac{\partial \phi}{\partial t} = -C_T \frac{\partial \sigma'_z}{\partial t} = -C_T \frac{\partial (p_l - p)}{\partial t}. \quad (2.3)$$

For most rock types, the Terzaghi compressibility  $C_T$  decreases rapidly during compaction. This type of compaction law is widely used in basin modeling. However, the formulation with only the vertical components of the stress tensor fails, when active extensional or compressional tectonics occur. Therefore, an extension of the law is proposed in Sec. 2.8.

Biot (1941) worked out a more detailed poro-elastic model for the extension of equation (2.1) for water filled porous rocks, taking into account the

effect of the rock compressibility  $C_r$ , which yields the following compaction law with the Biot compressibility  $C_B$ .

$$\frac{\partial \epsilon_v}{\partial t} = C_B \frac{\partial \sigma'}{\partial t} \quad \text{with} \quad \sigma' = \sigma - \alpha p \mathbf{I} \quad \text{and} \quad \alpha = 1 - \frac{C_r}{C_B} . \quad (2.4)$$

This formulation means, that the retardation of the compaction due to pore pressure drops with lower bulk compressibilities, since the rock compressibilities remain almost constant during compaction. Exceptions are mineral transformations or plastic flow of the grains. In unconfined sediments,  $C_r \ll C$  (soil mechanical approach) and  $\alpha \approx 1$ , while at large depth  $C_r \approx C_B \phi$  and  $\alpha \approx 1 - \phi$  (rock mechanical approach). The case  $\alpha = 1$  also means, that the effective stress is equal to the Terzaghi's assumption of negligible rock grain deformations. Note, that these effective stresses are only formal entities and not measurable physical values.

## 2.2 Terzaghi Type Models

Terzaghi type models are based on the simplifications of the lithostatic stress concept. In these models, overpressure formation related to incomplete mechanical compaction is considered and a fixed relation between porosity reduction and sediment compaction is assumed. The models have been widely used in 1D-Basin modeling programs since the early 90's. The assumptions are as follows:

- The "lithostatic pressure" concept is considered taking into account only the vertical component of the stress tensor as the maximum principal stress. The lithostatic pressure is equal to the overburden weight. The horizontal stresses are fixed ratios of the lithostatic pressure. Additional tectonic stresses, due to compressional or extensional forces, are neglected.
- Pore pressure formation is caused by overburden load. Fluid flow and compaction determine how the pressure is formed and distributed in the basin. Compaction is related to pore fluid outflow and decreases overpressure. One phase fluid flow in a fully saturated rock is considered, which is controlled by permeabilities. Pressure communication within the porous network is assumed.
- Mechanical compaction of the pore space takes into account the rearrangement of the grains to more compact blocks. All compaction is related to porosity reduction caused by pore fluid outflow. This porosity reduction process is controlled by the Terzaghi's effective stress value which is equal to the difference of the lithostatic and the pore pressure:  $\sigma' = \sigma_z - p$ . A relationship between maximum effective stress and porosity is assumed.
- Water is treated as incompressible.

### 2.2.1 Basic Formulation

#### Hydrostatic and Lithostatic Pressure

The hydrostatic pressure  $p_h$  at depth  $h$  is equal to the weight of a pure water column from sea level with the water density  $\rho_w$ .

$$p_h(h) = \int_0^h g \rho_w dz \quad (2.5)$$

with  $z = 0$  at sea level. This yields positive values below and negative values above sea level. The negative hydrostatic pressure at groundwater level is the groundwater potential. In basin modeling, the groundwater level is often assumed to be identical to the sediment surface.

The water density varies with changing salinity values, while the dependency on temperature and pressure is relatively small and often neglectable. A further simplification is the assumption of two constant densities for seawater  $\rho_{\text{sea}} = 1100 \text{ kg/m}^3$  and pore water  $\rho_w = 1040 \text{ kg/m}^3$ . This yields piecewise linear curves for hydrostatic pressure versus depth in sediments below sea water (Fig. 2.4).

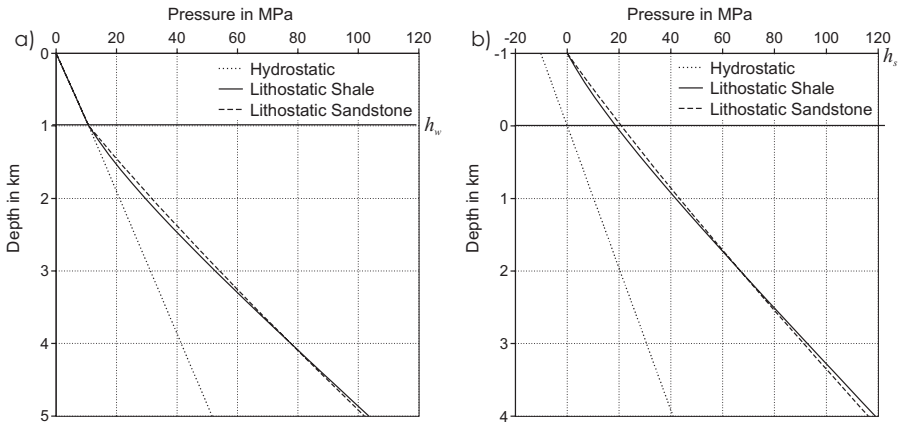


**Fig. 2.4.** Hydrostatic and lithostatic pressure curves for normal compacted rocks with the following properties: sea water density  $\rho_{\text{sea}} = 1100 \text{ kg/m}^3$ , pore water density  $\rho_w = 1040 \text{ kg/m}^3$ , shale density  $\rho_s = 2700 \text{ kg/m}^3$ , sandstone density  $\rho_s = 2720 \text{ kg/m}^3$ . (a) Offshore with a water depth  $h_w = 1 \text{ km}$ . (b) Onshore with a height of  $h_s = 1 \text{ km}$ . The lithostatic curves cross each other, since shale starts with a higher initial porosity but compacts faster

The lithostatic pressure  $p_l$  is equivalent to the total load of the overlying sediments of bulk density  $\rho_b$  and sea water. Lithostatic zero level is the surface onshore and the seawater level offshore.



$$\begin{aligned}
p_l(h) &= g \int_{h_s}^h \rho_b dz && \text{onshore} \\
p_l(h) &= g \int_0^{h_w} \rho_{\text{sea}} dz + g \int_{h_w}^h \rho_b dz && \text{offshore}
\end{aligned} \tag{2.6}$$

where  $h_s$  is the sediment surface. The integral over the weight of overburden sediments can be replaced by a sum of the weights of the single layers with thicknesses  $d_i$  ( $i$  is the layer number), rock densities  $\rho_{ri}$ , and and porosities  $\phi_i$ .

$$p_l(z) = \rho_{\text{sea}} g h_w + g \sum_{i=1}^n d_i [\rho_w \phi_i + \rho_{ri} (1 - \phi_i)] . \tag{2.7}$$

For a homogeneous sediment column with a constant rock density  $\rho_r$  equation (2.7) can further be simplified as follows:

$$\begin{aligned}
p_l(h) &= g \rho_{\text{sea}} h_w + g \rho_r (h - h_w) - g (\rho_r - \rho_w) \int_{h_w}^h \phi dz , && \text{onshore} \\
p_l(h) &= g \rho_r (h - h_s) - g (\rho_r - \rho_w) \int_{h_s}^h \phi dz , && \text{offshore.}
\end{aligned} \tag{2.8}$$

The remaining integral in the above equation is the weight percentage of water in the overlaying sediment column.

At larger depths, the term  $(1 - \phi)$  does not significantly change, which means the curve tends toward a straight line for a unique sediment type. Lithostatic pressure curves for shale and sandstone, for hydrostatic compaction with compaction parameters of Fig. 2.8, are shown in Fig. 2.4. The term lithostatic potential  $u_l$  is used for the lithostatic pressure minus hydrostatic pressure  $u_l = p_l - p_h$ .

## Pore Pressure Equation

The pore pressure equation is a one phase fluid flow equation based on the mass balance of pore water. A flow equation relates driving forces with flow rates. The driving force for pore water flow is the overpressure gradient. Darcys law establishes a linear relationship between the discharge velocity  $\mathbf{v}$  of the pore fluid and the overpressure gradient  $\nabla u$  assuming relatively slow flow for a Newtonian fluid. The proportionality factor is the mobility  $\boldsymbol{\mu} = \mathbf{k}/\nu$ , which is a function of the rock type dependent permeability  $\mathbf{k}$  and the fluid dependent viscosity  $\nu$ .

$$\mathbf{v} = -\frac{\mathbf{k}}{\nu} \nabla u . \tag{2.9}$$

This flow equation is an analogy to Fourier's equation of heat flow, which similarly relates temperature gradient and heat flux with the thermal conductivity tensor. The permeability tensor is often simplified using only two

values parallel and perpendicular to the facies layering, named as vertical and horizontal permeabilities.

Mass balance requires, that any fluid discharge from a volume element is compensated by change in the contained fluid mass. The internal fluid mass changes when the fluid density or the fluid volume is modified (App. B).

$$\nabla \cdot \mathbf{v} = -\frac{1}{1-\phi} \frac{\partial \phi}{\partial t} + \frac{1}{\rho} \frac{\partial \rho}{\partial t}. \quad (2.10)$$

Local changes of the fluid densities occur for fluid expansion processes like aquathermal pressuring, mineral transformations or petroleum generation and cracking. Changes in the fluid volume or porosity are related to mechanical and chemical compaction, which are considered as two independent processes.

The porosity reduction due to mechanical compaction is formulated with Terzaghi's compaction law, while chemical compaction induced porosity loss is a temperature and effective stress dependent function  $f_c(T, \sigma')$ , as specified later in Sec. 2.3.

$$\frac{\partial \phi}{\partial t} = -C \frac{\partial \sigma'_z}{\partial t} - f_c(T, \sigma'_z). \quad (2.11)$$

The basic model deals with mechanical compaction only and supposes Terzaghi's effective stress definitions, which yield the following pressure equation.

$$-\nabla \cdot \frac{\mathbf{k}}{\nu} \cdot \nabla u = -\frac{1}{1-\phi} \frac{\partial \phi}{\partial t} = \frac{C}{1-\phi} \frac{\partial \sigma'_z}{\partial t} = \frac{C}{1-\phi} \frac{\partial (u_l - u)}{\partial t}. \quad (2.12)$$

Thus,

$$\frac{C}{1-\phi} \frac{\partial u}{\partial t} - \nabla \cdot \frac{\mathbf{k}}{\nu} \cdot \nabla u = \frac{C}{1-\phi} \frac{\partial u_l}{\partial t}. \quad (2.13)$$

The equation shows that the overburden load causes overpressure increase and compaction. In the absence of all overpressure generating sources, fluid flow is still admissible, but then the total inflow is equal to the total outflow of each element. Pore water loss is always related to the corresponding overpressure discharge and the grain structure reacts instantaneously with mechanical compaction.

The two lithological parameters, compressibility and permeability control fluid flow and pressure formation. The bulk compressibility describes the ability of the rock framework to compact and it also controls how overburden influences pore pressure. The bulk compressibility in the pressure equation should not be mixed up with pure grain or fluid compressibility, which is orders of magnitude smaller. The higher the compressibility of the element the higher the pore pressure decrease and the smaller the overpressure formation. The permeability controls flow rates, flow paths, and the resulting pore pressure fields. The overpressure in an element cannot decrease if the elements surroundings are impermeable even when the element itself is highly permeable and compressible.

The permeability can vary by several orders of magnitude, ranging from highly permeable facies (sandstone) to low permeability facies (shale) to almost impermeable facies (salt). The two end members of almost impermeable and highly permeable facies are handled with special methods, which will be further discussed later in the 2D- and 3D-pressure examples.

Boundary values of equation (2.13) are overpressures and water flow velocities as illustrated in Fig. 2.5. The upper boundary condition is zero overpressure at the sediment–water–interface offshore and an overpressure equal to the groundwater potential at the sediment surface onshore. The groundwater potential yields topographic driven flow, which is explained in Sec. 2.2.5.

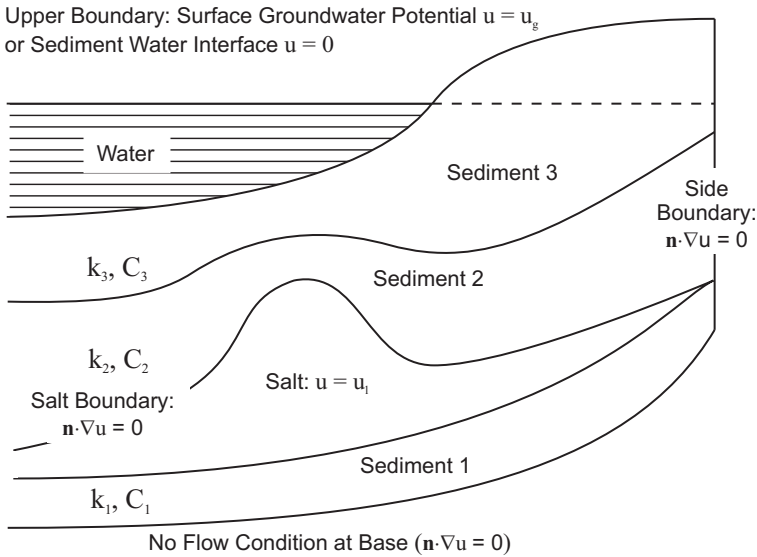


**Fig. 2.5.** Boundary value problem for overpressure calculation

The lower and side boundaries are no-flow areas, which means the overpressure gradient along the surface normal  $\mathbf{n}$  is set to zero  $\mathbf{n} \cdot \nabla u = 0$ . They are called closed boundaries. In small (prospect) scale models, special overpressures are usually set as side boundary values for some layers. For example, zero overpressure should be set at a permeable layer boundary, if it has a highly permeable connection to a hydrostatic area. To fix an overpressure value as a boundary condition at a certain point, is like injecting or releasing water until the given pressure is achieved. One can also apply a complete pressure array as side boundary values on prospect scale models from precalculated and calibrated basin scale models (Sec. 8.9). Special inner boundary conditions have to be set to impermeable rocks, namely no flow across the boundaries to these areas  $\mathbf{n} \cdot \nabla u = 0$  and lithostatic pressure within impermeable regions  $u = u_l$ .

## Compaction and Porosity Reduction

In the basic model, a simple relationship between mechanical compaction and porosity decrease is considered. Hence, the related porosity change is equivalent to the bulk strain and a function of the Terzaghi's effective stress. Several relationships between porosity and effective stress have been developed and they are described in the following section. Although the formulations look different, they are similar to exponential relationships of the following type:

$$\phi \approx k_1 e^{-k_2 \sigma'_z} . \quad (2.14)$$

The compaction in each volume element is usually realized with contraction of its vertical edges when only vertical compaction occurs. The relative decrease in any vertical length is equal to a relative decrease in volume. Then, the actual thickness  $d$  is calculated using any previous or initial thickness  $d_0$  from the present and previous porosities  $\phi$ ,  $\phi_0$  as follows:

$$\epsilon_z = \frac{d}{d_0} = \frac{1 - \phi_0}{1 - \phi} . \quad (2.15)$$

### 2.2.2 Mechanical Compaction

Mechanical compaction is almost irreversible. Hence, porosity is maintained when effective stress is decreased due to uplift, erosion, or an overpressure increase. The general porosity-effective stress relationship (2.14) could then still be used, but with the maximum effective stress value instead of the actual effective stress. This is taken into account when the following compaction laws are formulated in terms of effective stresses. Most mechanical compaction functions are porosity-effective stress relationships with decreasing porosity for increasing effective stress. The lithotype dependent functions can be measured through a triaxial compression test. Soil mechanical models use logarithmic functions between the void ratio  $e = \phi/(1 - \phi)$  and the effective stress, which yields a similar curve as equation (2.14).

$$e \approx k_1 - k_2 \log(\sigma'_z) . \quad (2.16)$$

The equivalence of the relationships (2.14) and (2.16) is illustrated in Fig. 2.6. The exponential porosity-effective stress has a wide range of linear porosity versus the logarithm effective stress relationship for most lithologies, and it also behaves almost linearly in the high porosity range when transformed into the corresponding void ratio diagram. Hence, the pure soil mechanical formulation should only be applied to an effective stress of 15 MPa or approximately 1 km.

Compaction curves generally depend on the stress path, but usually only normal compaction curves, with an uniform increase in overburden, are taken into account. Stress release caused by uplift and erosion shows an elastic

rebound, usually described with a low incline in the compaction diagram as illustrated in Fig. 2.6.

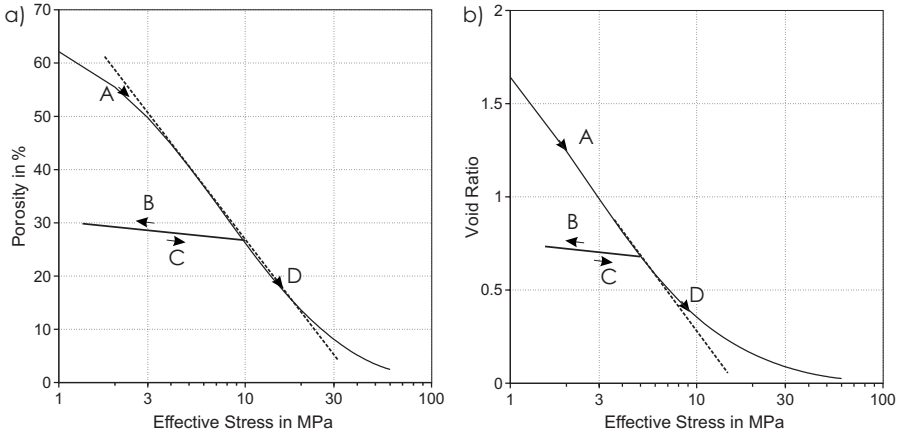


**Fig. 2.6.** Normal compaction curves (A and D) of a typical shale with an exponential porosity–effective stress relationship. The parameters are given in Fig. 2.8. The paths (B) and (C) represent load removal (erosion and uplift) and reload, respectively. (a) The porosity–stress relationship plotted versus the logarithmic stress axis has a wide range of linear behavior. (b) The void ratio–logarithm effective stress plot also behaves linearly for high porosities. The dashed curves represent linear approximations between porosity and void ratio and the logarithm of the effective stress

### Relationship between Effective Stress, Equivalent Hydrostatic Depth and Compressibility

The following compaction laws relate porosity to either effective stress  $\phi(\sigma'_z)$ , frame compressibility  $\phi(C)$ , or equivalent hydrostatic depth  $\phi(z_e)$ , which is the depth of the sample with the same porosity and rock type under hydrostatic pressure conditions. A formulation in terms of one of these independent variables can always be converted analytically or numerically into either of the others. A compaction law has to encompass all three relations during simulation:

- $\phi(\sigma'_z)$  determines new porosities after the pore pressure equation yields the effective stresses with the calculated new pore pressures.
- $C(\phi)$  or  $C(\sigma'_z)$  determines the actual frame compressibilities which are required in the pressure equation. The compressibility is the derivation of the  $\phi(\sigma'_z)$  function after  $\sigma'_z$ . It defines the slope of the porosity versus the effective stress curve.

- $\phi(z_e)$  is the theoretical porosity versus depth curve assuming hydrostatic pressures and the deposition of the entire column with the same lithotype. Many log and well data are available in terms of porosity versus equivalent hydrostatic depth rather than for porosity versus effective stress data. They are often used to determine the lithotype dependent parameters in the compaction laws.

Effective stress and compressibility based functions can simply be converted to each other by derivation or integration.

$$C(\sigma'_z) = -\frac{d\phi(\sigma'_z)}{d\sigma'_z}, \quad \phi(\sigma'_z) = -\int_0^{\sigma'_z} C(\sigma) d\sigma. \quad (2.17)$$

The hydrostatic porosity–depth function can be derived from the compressibility and porosity–effective stress equations as follows. For hydrostatic conditions, the effective stress change is equal to the change of the lithostatic minus the hydrostatic pressure

$$\frac{d\sigma'_z}{dz_e} = \Delta\rho g (1 - \phi) \quad (2.18)$$

where  $\Delta\rho = \rho_r - \rho_w$  is the difference of the rock and water density. Thus,

$$\frac{d\phi}{dz_e} = \frac{d\phi}{d\sigma'_z} \frac{d\sigma'_z}{dz_e} = -\Delta\rho g (1 - \phi) C(\phi). \quad (2.19)$$

The porosity–depth function can be analytically expressed if  $(1 - \phi)C(\phi)$  can be integrated. Analytical porosity–depth functions are very advantageous for the calibration of well data, but some relationships require numerical iteration schemes.

### Athy's Law formulated with Effective Stress

Athy (1930) proposed a simple exponential decrease of porosity with depth for a given rock type described only with an initial porosity  $\phi_0$  and a compaction parameter  $k$ . As already explained above, effective stress rather than total depth should be used in the compaction law. A corresponding simple exponential porosity–effective stress function was first proposed by Smith (1971).

$$\phi = \phi_0 e^{-k\sigma'_z}. \quad (2.20)$$

The compressibility function  $C(\phi)$  and the hydrostatic porosity–depth function  $\phi(z_e)$  are according to (2.17) and (2.19) as follows.

$$C(\phi) = k\phi, \quad (2.21)$$

$$\phi(z_e) = \frac{\phi_0}{\phi_0 + (1 - \phi_0) \exp(k\Delta\rho g z_e)}. \quad (2.22)$$

The exponential function (2.20) is a straight line in the logarithmic porosity versus effective stress diagram with  $k$  as the decline angle. Typical compaction curves for clastic rocks are shown in Fig. 2.7. The previous model can be easily extended with consideration of a non-zero minimum porosity  $\phi_m$ .

$$\phi = \phi_m + (\phi_0 - \phi_m) \exp(-k\sigma'_z), \quad (2.23)$$

$$C(\phi) = k(\phi_0 - \phi_m) \exp(-k\sigma'_z) = k(\phi - \phi_m), \quad (2.24)$$

$$\phi(z_e) = \frac{(\phi_0 - \phi_m) + \phi_m(1 - \phi_0) \exp(k(1 - \phi_m)\Delta\rho g z_e)}{(\phi_0 - \phi_m) + (1 - \phi_0) \exp(k(1 - \phi_m)\Delta\rho g z_e)}. \quad (2.25)$$

This model is frequently used in basin modeling (Giles et al., 1998), although the use of only one compaction parameter does not give a good match with observed data for many rock types.

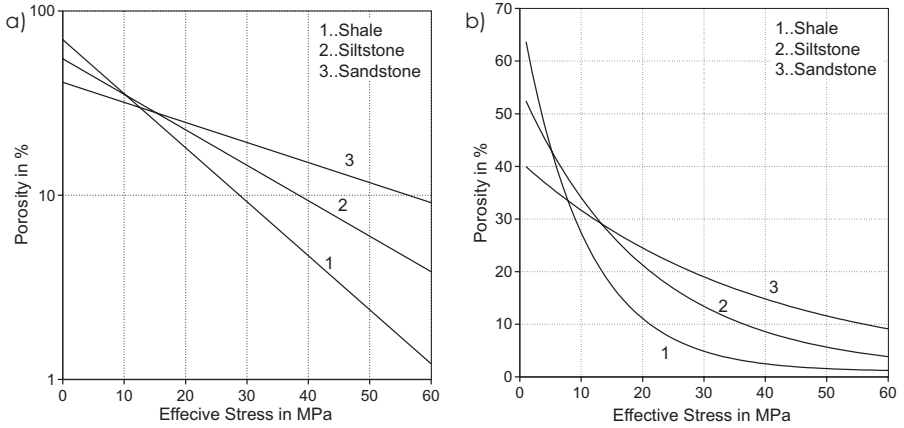


**Fig. 2.7.** Porosity versus effective stress curves on (a) logarithmic and (b) linear scale for various lithologies using Athy's Effective Stress law with the following parameters: shale  $\phi_0 = 0.70$ ;  $k = 0.096 \text{ MPa}^{-1}$ , siltstone  $\phi_0 = 0.55$ ;  $k = 0.049 \text{ MPa}^{-1}$ , sandstone  $\phi_0 = 0.41$ ;  $k = 0.0266 \text{ MPa}^{-1}$ . The minimum porosity is zero

### Athy's Law formulated with Hydrostatic Depth

A depth related porosity law (Athy, 1930) is used with the introduction of an equivalent hydrostatic depth  $z_e$  instead of the total depth.

$$\phi = \phi_0 \exp(-kz_e). \quad (2.26)$$

The advantage of this formulation is, that the compaction parameter  $k$  can be easily determined when measured porosity versus equivalent depth data

is available. The compressibility function  $C(\phi)$  and the hydrostatic porosity–depth function  $\phi(z_e)$  are according to (2.17) and (2.19) as follows.

$$C = \frac{k}{\Delta \rho g} \frac{\phi}{(1 - \phi)}, \quad (2.27)$$

$$\sigma'_z(\phi) = \frac{\Delta \rho g}{k} \left( \phi - \phi_0 - \ln \frac{\phi}{\phi_0} \right). \quad (2.28)$$

The inverse function  $\phi(\sigma')$  can be calculated with the Newton iteration method. The resulting porosity–effective stress curves are generally steeper in the high porosity and shallower in low porosity ranges than the Athy versus effective stress functions. Hence, they are more applicable for most rock types even though they are based on only one compaction parameter. The authors prefer this law as a default for most lithologies. Example compaction curves for clastic rocks and carbonates are illustrated in Fig. 2.8.

### Schneider Model

An extension of Athy’s effective stress law to two exponential terms was proposed by Schneider et al. (1996).

$$\phi = \phi_1 + \phi_a \exp(-k_a \sigma'_z) + \phi_b \exp(-k_b \sigma'_z). \quad (2.29)$$

Different compaction parameters  $k_a$ ,  $k_b$  for lower and higher porosity ranges are realized with the superposition of two exponential terms. The initial porosity is equal to the sum of the three porosity parameters  $\phi_1 + \phi_a + \phi_b$ . Both porosities  $\phi_a$  and  $\phi_b$  are usually assumed to be half of the initial porosity value  $\phi_0$ .

The corresponding compressibility function is as follows:

$$C(\sigma'_z) = k_a \phi_a \exp(-k_a \sigma'_z) + k_b \phi_b \exp(-k_b \sigma'_z). \quad (2.30)$$

The hydrostatic porosity versus depth function can be obtained, when equation (2.18) is integrated numerically to get  $\sigma'_z(z_e)$ , and then  $\phi(z_e)$  is calculated with equation (2.29) afterwards. Numerical integration can also be applied to any other model with a given analytical expression for  $\phi(\sigma'_z)$ . The proposed default parameters in App. A yield curves almost identical to those of Athy’s depth model (Fig. 2.8).

### Compressibility Model

Compressibilities are the derivatives of the porosity versus effective stress and are proportional to the slope of the porosity versus effective stress curves. This model assumes an exponential decrease in the compressibilities from the depositional value  $C_0$  to a value  $C_m$  corresponding to the minimum porosity  $\phi_m$  (Fig. 2.9).



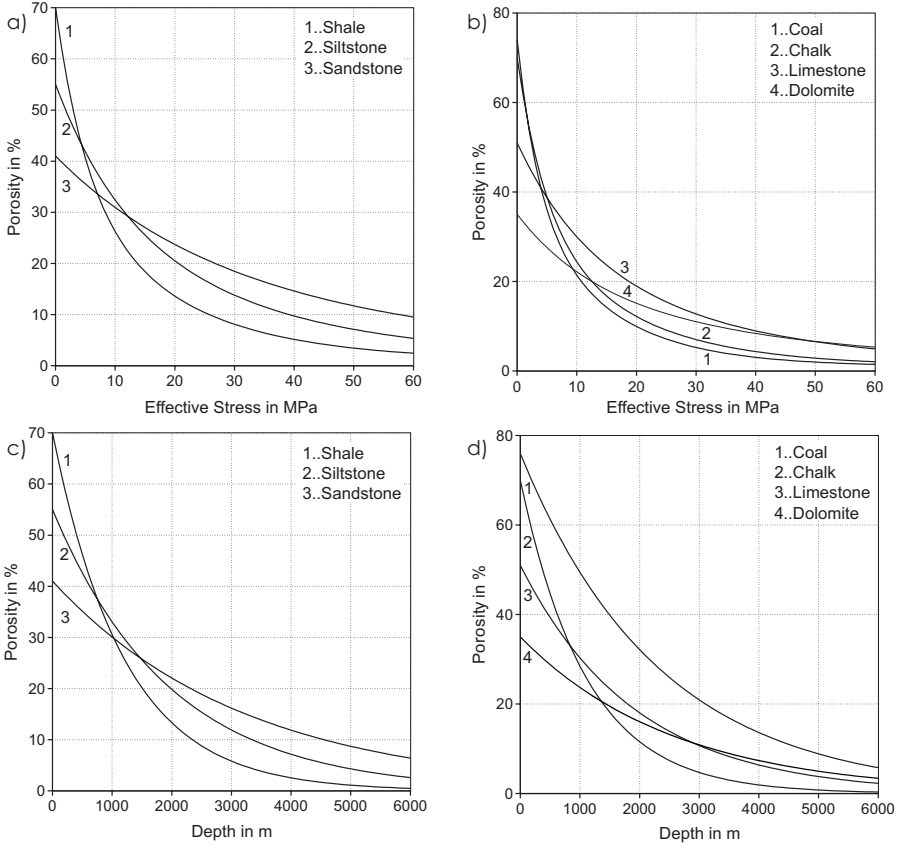


**Fig. 2.8.** Porosity versus hydrostatic depth and effective stress curves for various lithologies using Athy's depth law with the following parameters: shale  $\phi_0 = 0.70, k = 0.83 \text{ km}^{-1}$ , siltstone  $\phi_0 = 0.55, k = 0.34 \text{ km}^{-1}$ , sandstone  $\phi_0 = 0.41, k = 0.31 \text{ km}^{-1}$ , coal  $\phi_0 = 0.76, k = 0.43 \text{ km}^{-1}$ , chalk  $\phi_0 = 0.70, k = 0.90 \text{ km}^{-1}$ , limestone  $\phi_0 = 0.51, k = 0.52 \text{ km}^{-1}$ , dolomite  $\phi_0 = 0.70, k = 0.39 \text{ km}^{-1}$

$$\log C(\phi) = \frac{\phi_0 - \phi}{\phi_0 - \phi_m} \log C_m + \frac{\phi - \phi_m}{\phi_0 - \phi_m} \log C_0. \quad (2.31)$$

This is equivalent to the following expression:

$$C(\phi) = \alpha \exp(\beta \phi) \quad \text{with} \quad (2.32)$$

$$\ln(\alpha) = \frac{\phi_0 \ln C_m - \phi_m \ln C_0}{\phi_0 - \phi_m}, \quad \beta = \frac{\ln C_0 - \ln C_m}{\phi_0 - \phi_m}.$$

Integration of the above exponential function yields the corresponding effective stress correlations.

$$\begin{aligned}\phi(\sigma'_z) &= -\frac{1}{\beta} \ln(\alpha\beta\sigma'_z + \exp(-\beta\phi_0)) \\ C(\sigma'_z) &= \frac{\alpha}{\alpha\beta\sigma'_z + \exp(-\beta\phi_0)}.\end{aligned}\quad (2.33)$$

Numerical integration of (2.19) can be used to determine the hydrostatic porosity versus depth function  $\phi(z_e)$  from  $C(\sigma'_z)$ . Compressibility models generally decrease too fast for low porosities. Default parameters are shown in Appendix A and the curves for clastic rocks are illustrated in Fig. 2.9.

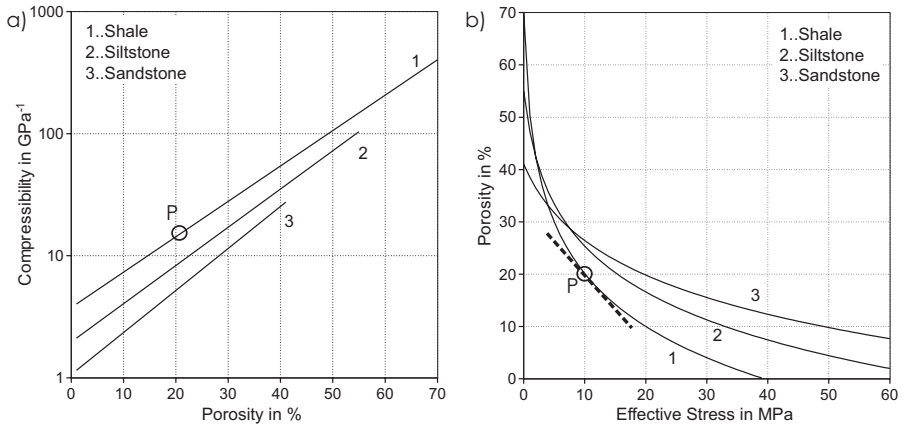


**Fig. 2.9.** Compaction curves for various lithologies using the compressibility model with the following parameters: Shale  $C_0 = 403 \text{ GPa}^{-1}$ ,  $C_m = 4.03 \text{ GPa}^{-1}$ , Siltstone  $C_0 = 103 \text{ GPa}^{-1}$ ,  $C_m = 2.11 \text{ GPa}^{-1}$ , Sandstone  $C_0 = 27.5 \text{ GPa}^{-1}$ ,  $C_m = 1.15 \text{ GPa}^{-1}$

## Mudstone Model

The following law from soil mechanics is especially applicable for clastic rocks.

$$e = \frac{\phi}{1 - \phi} = e_{100} - \beta \log \frac{\sigma'_z}{0.1 \text{ MPa}}. \quad (2.34)$$

The reference void ratio  $e_{100}$  at 0.1 MPa can be considered as an initial void ratio  $e_{100} = \phi_0 / (1 - \phi_0)$  although this compaction law yields a singularity  $e \rightarrow \infty$  for the void ratio at zero stress. The two functions  $\phi(\sigma'_z)$  and  $C(\sigma'_z)$  are as follows.

$$\phi(\sigma'_z) = \frac{\sigma'_z - \beta \log(\sigma'_z / 0.1 \text{ MPa})}{1 + e_{100} - \beta \log(\sigma'_z / 0.1 \text{ MPa})}, \quad (2.35)$$

$$C(\sigma'_z) = \frac{\beta}{\sigma'_z(1 + e_{100} - \beta \log(\sigma/0.1 \text{ MPa})^2)} . \quad (2.36)$$

The above model does not provide an analytical expression for the porosity-depth function. However, with the compressibility model equation (2.19), it can be integrated numerically.

The material dependent constants are the initial void ratio  $e_{100}$  and the compressibility  $\beta$ . They can be related to the (volumetric) clay content  $r$  for mudstones with the following relationships proposed by Yang and Aplin (2004) Fig. 2.10.

$$\begin{aligned} e_{100}(r) &= 0.3024 + 1.6867 r + 1.9505 r^2 \\ \beta(r) &= 0.0937 + 0.5708 r + 0.8483 r^2 . \end{aligned} \quad (2.37)$$

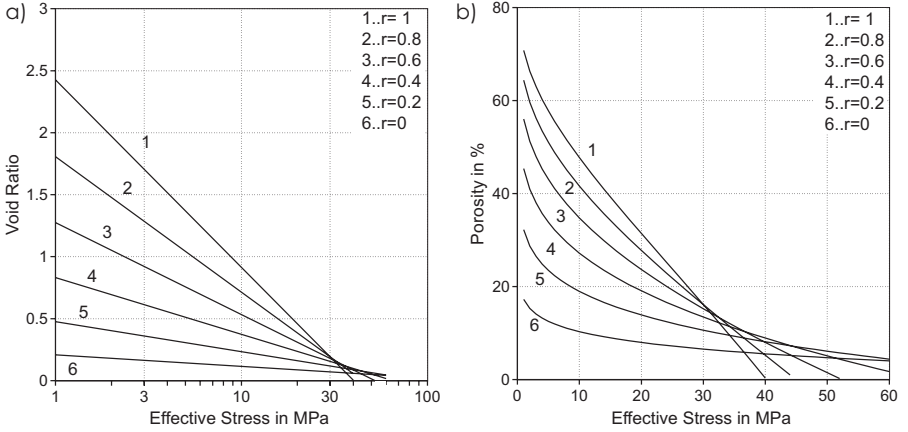


**Fig. 2.10.** Compaction curves for various lithologies using the mudstone model with the clay dependent functions of Yang and Aplin

Lauvrak (2007) proposed the EasySoil model with the following correlations to sample data for  $e_{100}^*$ ,  $\beta^*$  and an upscaling to  $e_{100}$ ,  $\beta$  for natural rocks (Fig. 2.11).

$$\begin{aligned} e_{100}^*(r) &= 0.725 - 0.252 r + 2.53 r^2, \\ \beta^*(r) &= 0.218 - 0.119 r + 1.193 r^2, \\ e_{100} &= e_{100}^* + 0.76 \beta^*, \\ \beta &= 1.07 \beta^* . \end{aligned} \quad (2.38)$$

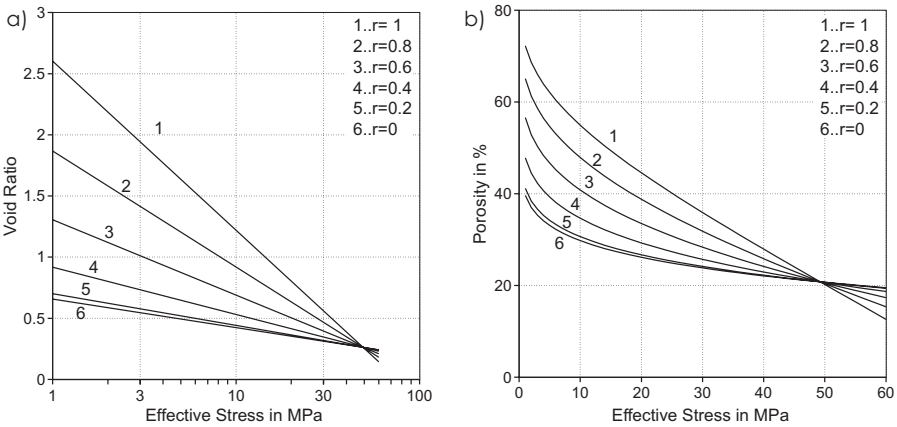


**Fig. 2.11.** Compaction curves for various lithologies using the mudstone model with the clay dependent functions of Lauvraks EasySoil model

Compressibilities

Bulk compressibilities can be directly derived from the compaction law as previously explained. Example curves for clastic rocks and carbonates are shown in Fig. 2.12 with the parameters of the Athy’s hydrostatic depth model. Other compaction models yield similar curves with the proposed default parameters.

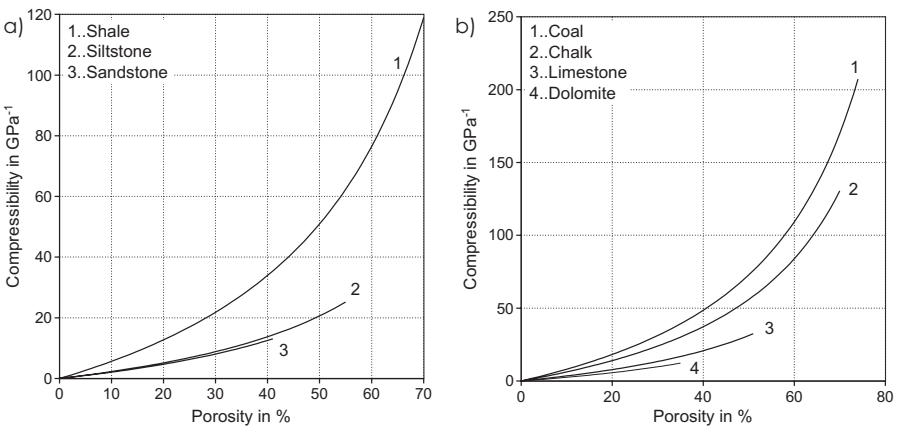
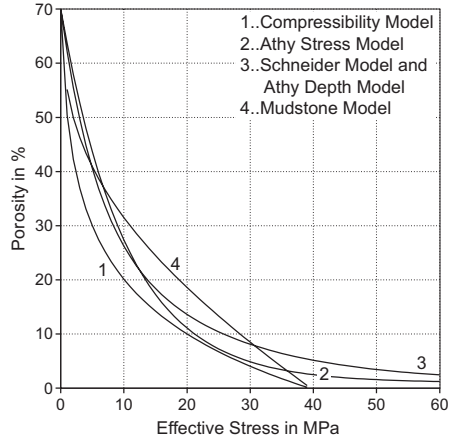


**Fig. 2.12.** Compressibility curves for various lithologies using Athy’s depth law with the parameters of Fig. 2.8

## Comparison of Various Lithologies

Although the formulation of the various compaction models look very different from each other, default parameters for most lithologies yield very similar compaction curves. An exception is the mudstone model, which is generally not suitable for approximation of the compaction trend in the lower porosity range. The standard shale curves are shown in Fig. 2.13 for all described models. The compaction parameters are mixed arithmetically. Example curves for shale–sandstone mixtures are shown in Fig. 2.14.

**Fig. 2.13.** Comparison of different compaction laws for shale: The curves for the Schneider and Athy's depth model are almost identical and plotted in one line. (1) Compressibility model:  $C_0 = 403 \text{ GPa}^{-1}$ ,  $C_m = 4.03 \text{ GPa}^{-1}$  (2) Athy's effective stress law:  $\phi_0 = 0.70$ ,  $k = 0.096 \text{ MPa}^{-1}$  (3) Schneider model:  $\phi_0 = 0.70$ ,  $\phi_a = 0.35$ ,  $k_a = 0.1916 \text{ MPa}^{-1}$ ,  $k_b = 0.0527 \text{ MPa}^{-1}$  and Athy's hydrostatic depth law:  $k = 0.83 \text{ km}^{-1}$  (4) Mudstone model:  $e_{100} = 1.2889$ ,  $\beta = 0.458$



### 2.2.3 Permeability and Viscosity

The mobility  $\mu$  is a measure of the ability of a material to transmit fluids. It includes the rock permeability  $k$  and the fluid viscosity  $\nu$ :  $\mu = k/\nu$ . In the Darcy law (2.9), the mobility is the proportional factor between pressure gradients and fluid flow velocities. This applies to slow flowing (Newtonian) fluids. The permeability is mainly affected by the pore structure of the rock, and the viscosity describes the internal friction of the moving phase. This indicates that flow velocity rises with rising permeability and reduces with increasing viscosity.

#### Viscosity

Fluid viscosity is a measure of the resistance of the fluid against flow. It is related to the attractive forces between the molecules. Viscosity generally depends on pressure, temperature, and phase composition. The considered viscosity is the dynamic viscosity  $\nu$  in contrast to the kinematic viscosity  $\nu/\rho$ . The unit of the dynamic viscosity is Poise (P,  $1 \text{ Pa s} = 0.1 \text{ P}$ ).

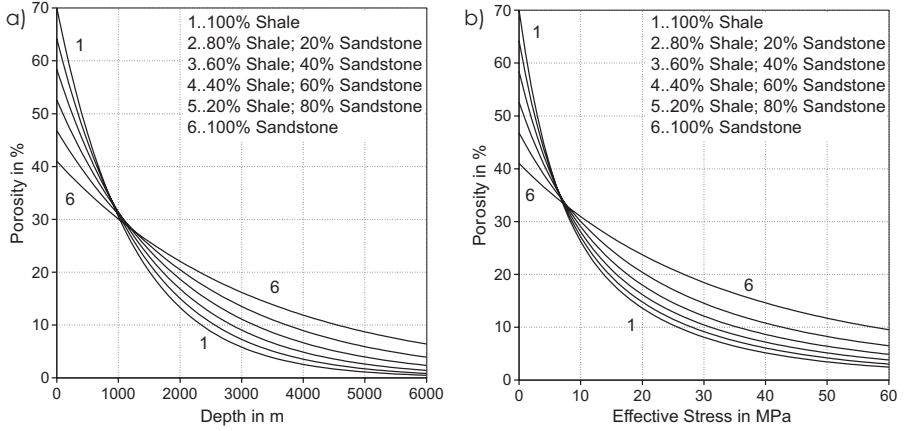


**Fig. 2.14.** Compaction curves for mixtures of shale and sandstone using arithmetic averages of all compaction parameters. (a) Athy's depth model with shale  $\phi_0 = 0.70, k = 0.83 \text{ km}^{-1}$  and sandstone  $\phi_0 = 0.41, k = 0.31 \text{ km}^{-1}$ . (b) Schneider model with shale  $\phi_0 = 0.70, \phi_a = 0.35, k_a = 0.1916 \text{ MPa}^{-1}, k_b = 0.0527 \text{ MPa}^{-1}$  and sandstone  $\phi_0 = 0.42, \phi_a = 0.205; k_a = 0.0416 \text{ MPa}^{-1}, k_b = 0.0178 \text{ MPa}^{-1}$

The viscosity of saline water can be estimated from McCain Jr. (1990) in Danesh (1998) as follows:

$$\begin{aligned} \nu &= \nu_T (0.9994 + 4.0295 \times 10^{-5} P + 3.1062 \times 10^{-9} P^2) \\ \nu_T &= T^{-a} (109.547 - 8.40564 s + 0.313314 s^2 + 8.72213 \times 10^{-3} s^3) \\ a &= 1.12166 - 2.63951 \times 10^{-2} s + 6.79461 \times 10^{-4} s^2 \\ &\quad + 5.47119 \times 10^{-5} s^3 - 1.55586 \times 10^{-6} s^4 \end{aligned} \quad (2.39)$$

with  $\nu$  in mPas,  $T$  in  $^{\circ}\text{F}$ ,  $P$  in psi,  $s$  in mass %, and the validity intervals for  $\nu_T$  of  $38^{\circ}\text{C} < T < 200^{\circ}\text{C}$  and  $s < 26\%$ , and for  $\nu$  of  $30^{\circ}\text{C} < T < 75^{\circ}\text{C}$ , and  $P < 100 \text{ MPa}$ .

Another formulation was published by Hewlett-Packard (1985) in Mc Dermott et al. (2004).

$$\begin{aligned} \nu &= \nu_0 [1 - 1.87 \times 10^{-3} s^{0.5} + 2.18 \times 10^{-4} s^{2.5} \\ &\quad + (T^{0.5} - 0.0135 T)(2.76 \times 10^{-3} s - 3.44 \times 10^{-4} s^{1.5})] \\ \nu_0 &= 243.18 \times 10^{-7} 10^{247.8/(T_K - 140)} \\ &\quad [1 + 1.0467 \times 10^{-6} P (T_K - 305)] \end{aligned} \quad (2.40)$$

with  $\nu$  in mPas,  $T$  in  $^{\circ}\text{F}$ ,  $T_K$  in K,  $P$  in bar,  $s$  in %, and the validity interval  $0^{\circ}\text{C} < T < 300^{\circ}\text{C}$ ,  $s < 25\%$  and  $P < 430^{\circ}\text{C}$ . In the published equation  $P$  is

the difference between the real and the saturation pressure, but the latter one can be neglected for geological conditions.

Both formulations yield similar results for moderate pressures (Fig. 2.15). The uncertainties of mobilities are controlled more by permeability than viscosity. Hence, the following simplification of equation (2.39) without salinity and pressure dependence is also proposed here (dotted curve in Fig. 2.15.a).

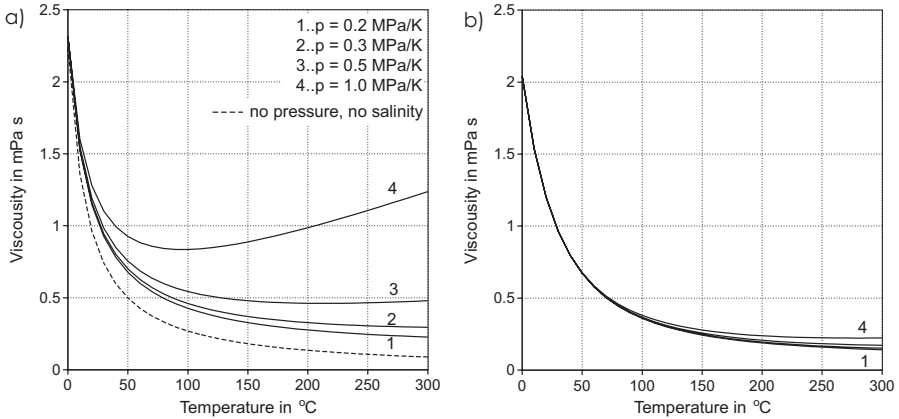


**Fig. 2.15.** Pressure and temperature dependent water viscosity curves assuming a salinity of 10% after (a) McCain Jr. (1990) in Danesh (1998) and (b) Hewlett-Packard (1985) in Mc Dermott et al. (2004). The pressure and salinity independent curve for the simplified equation (2.41) is the dashed curve in (a)

$$\nu[\text{cp}] = 109.5 T^{-1.122} \quad (2.41)$$

with temperature  $T$  in  $^{\circ}\text{F}$ . The viscosity of liquid and vapor petroleum is dependent on its composition. Viscosity ranges for standard oils and gases and more sophisticated methods for calculating oil and gas viscosities from compositions are described in (Sec. 5.6.5).

## Permeability

Permeability consists of two factors namely rock (intrinsic) permeability and relative permeability, the latter one is further described in Sec. 6.3. The intrinsic permeability  $k$  is mainly affected by the pore structure, especially pore throat diameters and pore connectivity. Hence, it is dependent on the compaction state and usually tabulated as a function of porosity (App. A). The unit of permeability is Darcy ( $1 D = 0.98692 \times 10^{-12} \text{ m}^2$ ), or millidarcy (mD), but logarithm millidarcy (log mD) is also used, since permeability values often vary over orders of magnitude with decreasing porosity ( $1 \text{ log mD} = 10 \text{ mD}$ ,  $0 \text{ log mD} = 1 \text{ mD}$ ,  $-1 \text{ log mD} = 0.1 \text{ mD}$ ,  $-2 \text{ log mD} = 0.01 \text{ mD}$ , ...).

The most commonly used permeability relationship is the Kozeny–Carman relation. A derivation can be drafted from Hagen–Poiseuille’s law for fluid flow through a porous structure, which is approximated by a bundle of tubular parallel capillaries.

The flow velocity of a viscous fluid of  $N$  parallel tubes of radius  $r$  embedded in an rock matrix of bulk area  $A$  can be expressed with the Hagen–Poiseuille law as follows.

$$\mathbf{v} = \frac{N}{A} \frac{r^4 \pi}{8\nu} \nabla p \quad (2.42)$$

where  $\nabla p$  is the driving pressure gradient along the tubes. The porosity of the considered tubular bundle is  $\phi = N\pi r^2/A$ , which yields the following fluid velocity.

$$\mathbf{v} = \frac{r^2 \phi}{8\nu} \nabla p . \quad (2.43)$$

The comparison with Darcy’s Law (2.9) results in a permeability of  $k = r^2 \phi / 8$ . The introduction of a tortuosity  $\tau$ , which is defined as “the length of the path actually followed between two points divided by the apparent path between these two points” (Vidal-Beaudet and Charpentier, 2000) or as “the averaged ratio of path-lengths traveled by a petroleum fluid to the geometrical length of the region of rock considered” (England et al., 1987) yields

$$k = \frac{r^2 \phi}{8\tau^2} . \quad (2.44)$$

It can be estimated with  $\tau = \sqrt{3}$  for many rocks.

This equation can be rewritten to a so called Kozeny–Carman type relationship of the form

$$k = \frac{B\phi^3}{\tau^2 S^2} \quad (2.45)$$

with the specific surface area  $S = N2\pi r/A$  and  $B$  a geometrical factor (Mavko et al., 1998).

From consideration of sphere packing it is possible to estimate  $S = (3/2)(1 - \phi)/d$  with  $d$  as grain size. Furthermore, it is common, to replace the porosity  $\phi$  with  $(\phi - \phi_c)$  by assuming that the permeability vanishes below a threshold porosity  $\phi_c$  where the pores become unconnected (Mavko et al., 1998).

However, the following revised Kozeny–Carman relationship has been proposed by Ungerer et al. (1990) for practical use in basin modeling.

$$\begin{aligned} k(\phi) &= 2 \times 10^{16} \kappa \frac{\phi'^5}{S^2(1 - \phi')^2} & \text{if } \phi' < 0.1 \\ k(\phi) &= 2 \times 10^{14} \kappa \frac{\phi'^3}{S^2(1 - \phi')^2} & \text{if } \phi' > 0.1 \end{aligned} \quad (2.46)$$



with specific surface area  $S$  in  $\text{m}^2/\text{m}^3$ ,  $\kappa$  a lithotype dependent scaling factor and  $\phi'$  a corrected porosity  $\phi' = \phi - 3.1 \times 10^{-10}S$ . Example parameters for clastic rocks are given in Table 2.2.

Lithology	Specific Surface Area in $\text{m}^2/\text{m}^3$	Scaling Factor
Shale	$10^8$	0.01
Siltstone	$10^7$	0.5
Sandstone	$10^6$	10.0

**Table 2.2.** Kozeny–Carman parameters for various lithologies

The Kozeny–Carman type relation (2.46) has two different exponential factors for the high and low porosity range. The permeability decrease for highly porous rocks is mainly caused by the reduction of the pore throat radius, while in the highly compacted rocks, the closure and elimination of pore throats yields a decrease in pore connectivity (coordination number) and a drop in permeability.

However, all Kozeny–Carman type models describe the intrinsic permeability dependent on porosity, pore size, pore throat radii distribution, and coordination number, which is a measure of the pore connectivities. Further considerations based on more complex geometrical models are e.g. given in Vidal-Beaudet and Charpentier (2000), Doyen (1988).

An alternative approach describes the permeability with a piecewise linear function in the log permeability versus porosity diagram. Example curves for many lithologies are tabulated in App. A in terms of three porosity versus log permeability pairs. Some of these curves for clastic rocks and carbonates together with the corresponding Kozeny–Carman curves with the parameters from Table 2.2 are illustrated in Fig. 2.16. Salt, granite and basalt are considered as impermeable.

Permeabilities are mixed geometrically for homogeneous mixtures or lithotypes. In layered mixtures the horizontal values are mixed arithmetically and the vertical values are mixed harmonically.

Generally, permeability  $\mathbf{k}$  is a symmetrical tensor with six independent components. Similar to the thermal conductivity, it is often approximated with only two independent components: the permeability along the geological layer  $k_h$  and permeability across the geological layer  $k_v$  with an anisotropy factor  $a_k = k_h/k_v$ . Typical anisotropy values are  $a_k = 2 \dots 10$  for clastic rocks and  $a_k = 1 \dots 3$  for carbonates, they are tabulated for many rock types in App. A.

The above permeability curves and tabulated permeability values mean vertical permeabilities and equivalent hand-sample values, since most published data and in-house databases in oil companies are derived from hand-sample measurements. Basin scale values for horizontal and vertical perme-

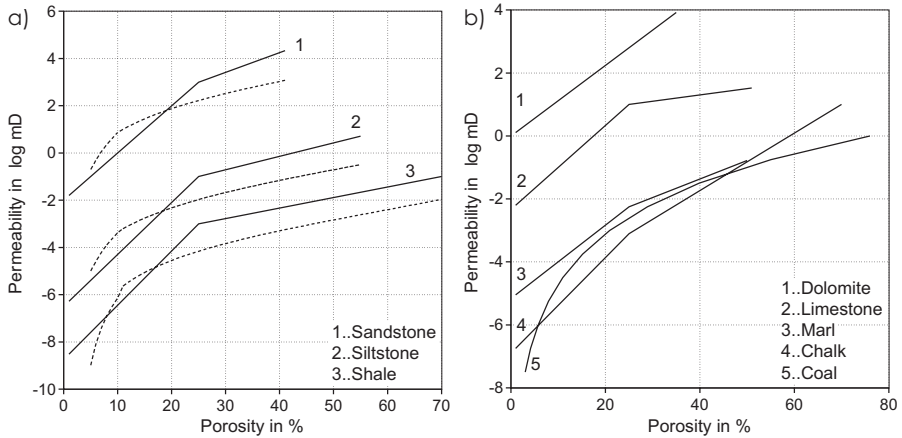


**Fig. 2.16.** Permeability curves for various lithologies with piecewise linear (solid) and Kozeny–Carman (dashed) relationships. The parameters are from Table 2.2 and from the Appendix A. A special curve is proposed for coal

abilities are calculated from the hand specimen values multiplied with a horizontal and vertical upscaling factor, respectively. The higher values for larger scales are caused by macro-fractures, inhomogeneities and permeable inclusions. Upscaling factors to basin scale elements with lengths greater than 50 m are reported for sandstones: 500 (horizontal) and 10 (vertical) (Schulze-Makuch et al., 1999). Based on the authors' experience, we suggest upscaling factors of 50 (horizontal) and 1 (no upscaling vertical) for all clastic rocks and carbonates, and no upscaling otherwise. Different horizontal to vertical upscaling increases the anisotropy factor in clastic rocks to  $a_k = 100 \dots 500$ , respectively.

The permeability of fractured rock is much higher than that of undisturbed samples and is discussed in Sec. 2.6.1.

## 2.2.4 1D Pressure Solutions

Simplified 1D models can be used to discuss some fundamental processes of overpressure formation and compaction, although 1D solutions are less practical, since most overpressure distributions are strongly influenced by horizontal water flows along highly permeable layers (App. D). In this section, only mechanical compaction is considered in describing the interaction of overburden due to sedimentation, overpressure formation and compaction. The 1D formulation of the general pressure equation (2.13) is as follows.

$$C \frac{\partial u}{\partial t} - \frac{k}{\nu} \frac{\partial u}{\partial z} = C \frac{\partial u_l}{\partial t}. \quad (2.47)$$

Pressure curves for a unique rock type deposited with constant sedimentation rates are shown in Fig. 2.17 for shales and siltstones. Shale permeability decreases rapidly during burial, since the log permeability to porosity curve is very steep. Hence, there is only a small sedimentation rate dependent transition zone between the uppermost 1...3 km and the deeper part, where the pressure gradient is equal to the lithostatic gradient. The transition zone in lower permeable rocks like siltstone occurs over a broader region of sometimes several kilometers. The corresponding porosity curves for homogeneous depositions are shown in Fig. 2.18. The porosity reduction stops in the deep impermeable blocks, when water outflow is near zero.

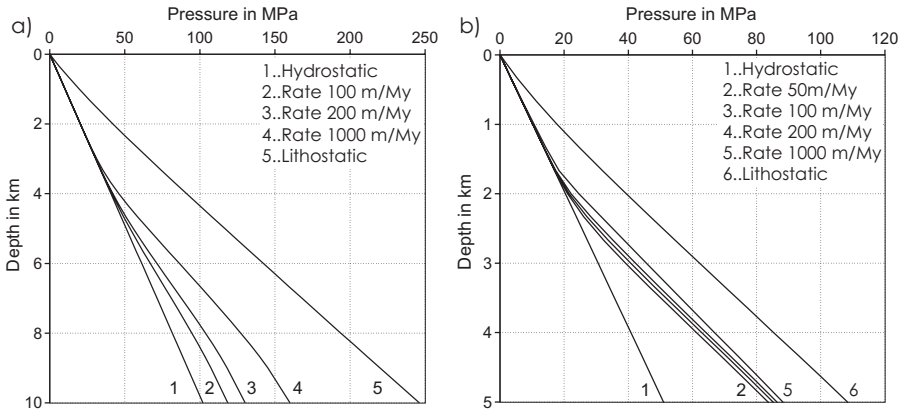


**Fig. 2.17.** Sedimentation rate dependent overpressure formation of (a) siltstones and (b) shales with piecewise linear permeability curves of Fig. 2.16

The pressure formation in an alternating sandstone–shale sequence is shown in Fig. 2.19. The pressure gradient in sandstone is equal to the hydrostatic gradient, while the pressure in the shale layer returns relatively quickly (after 500 m in the example) to almost the level of the pure shale curve. Hence, the increase of pressure in seals could be much higher than the lithostatic gradients.

The behavior of an impermeable seal is illustrated in Fig. 2.20. All overburden load above the seal is added to the pore pressure of all layers below the seal, since no pore water can cross the impermeable seal. This yields an increase to lithostatic pressure in the seal and a constant offset equal to the overburden load of the overpressure below the seal during the time after the sedimentation of the seal. This displacement with additional pressure is marked with the dotted line in Fig. 2.20.b. The pore pressure (solid line) also includes a small pressure exchange within the block below the seal.

The following calculation shows reservoir pressure decrease by water flow through a permeable seal (Fig. 2.21). The considered reservoir has a thickness

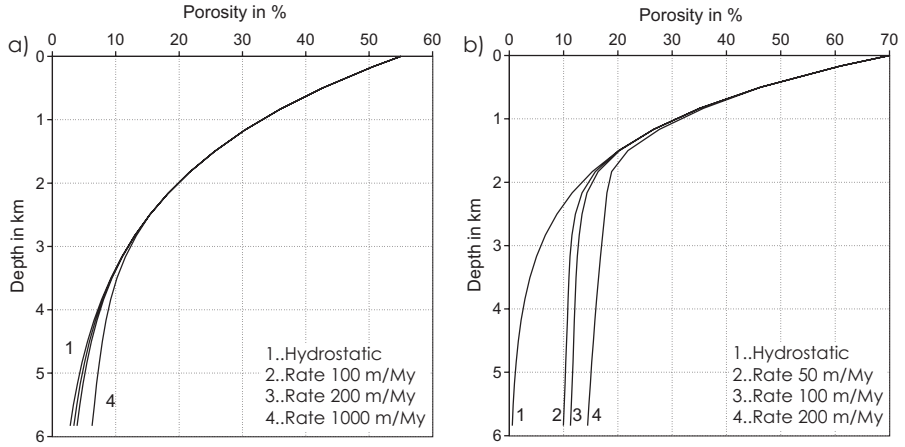


**Fig. 2.18.** Sedimentation rate dependent compaction of (a) siltstones and (b) shales with compaction curves of Fig. 2.8

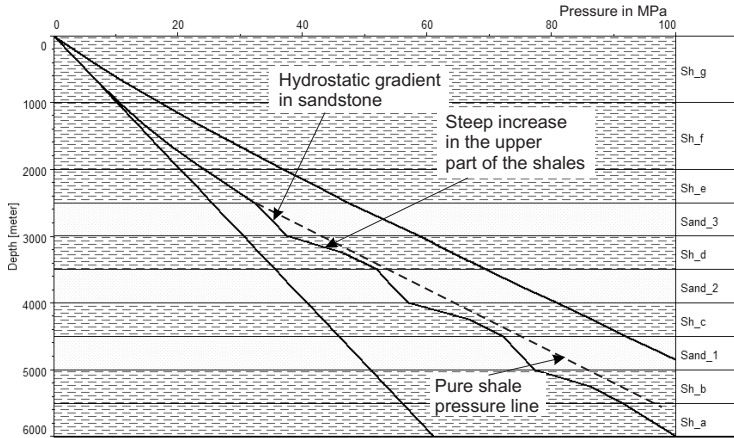


**Fig. 2.19.** 1D overpressure formation in an alternating sand-shale sequence

$h_r$ , a bulk compressibility  $C_r$  and an overpressure  $u_r$ . The overpressure in the seal with a permeability  $k_s$  and a thickness  $h_s$  drops to zero at or near the top of the seal. The flow velocity in the seal is according to the Darcy's law as follows.

$$v = \frac{k_s}{\nu} |\nabla u| \approx \frac{k_s}{\nu} \frac{u_r}{h_s} . \quad (2.48)$$

Integration of equation (2.13) over the reservoir area with the assumption of no sedimentation yields the following relationship.

$$\int \mathbf{v} \cdot \mathbf{n} dS = \int C \frac{\partial u}{\partial t} dV . \quad (2.49)$$

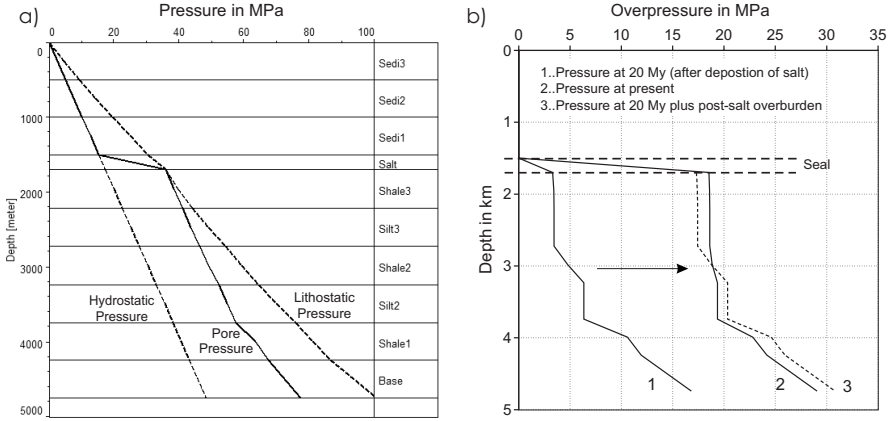


**Fig. 2.20.** 1D overpressure formation below a perfect seal. (a) Present day pressure versus depth curve. (b) Overpressure versus depth curves for the time of seal deposition and at present day. The pressure curve at seal deposition (20 My) is shifted to the corresponding present day locations to illustrate, that overpressure increase in all layers below the seal from 20 My to present day is almost the same. The dashed curve is the 20 My curve plus the overburden load after seal deposition. The difference of the dashed curve and the present day overpressure curve is caused by water exchange in the layers below the seal

The outflow of the reservoir is restricted to the reservoir–seal interface with surface  $A_r$ . Hence,

$$A_r v = -C_r V_r \frac{\partial u}{\partial t} \quad (2.50)$$

with the reservoir volume  $V_r = A_r h_r$ . Thus,

$$\frac{\partial u_r}{\partial t} = -\frac{k_s}{C_r \nu h_s h_r} u_r. \quad (2.51)$$

It yields an exponential decrease in the reservoir pressure as follows.

$$u_r(t) = u_0 \exp\left(-\frac{t}{\tau}\right), \quad \tau = \frac{C_r \nu h_s h_r}{k_s}. \quad (2.52)$$

with an initial reservoir pressure  $u_0$ . The time  $t_h = \tau \ln(2)$  when half of the overpressure is dropped is controlled by the permeability of the seal, the bulk compressibility of the reservoir, and the reservoir and seal thicknesses. Typical values for  $t_h$  (Fig. 2.22) show, that very low permeabilities are necessary to seal pressure over significant times.

### 2.2.5 Pressure Solutions in 2D and 3D

Most of the effects discussed in the previous sections are also important in multidimensional pressure calculations: the upper part of the basin is in a

**Fig. 2.21.** Overpressure formation and decrease below a permeable seal. It is assumed, that the overpressure in a permeable seal drops linearly from reservoir pressure to zero. The overpressure in the compartment is constant. The water flow through the seal and the related decrease in reservoir pressure depend on seal permeability, reservoir compressibility and the thicknesses of the two layers

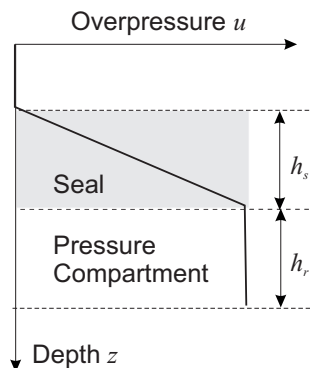
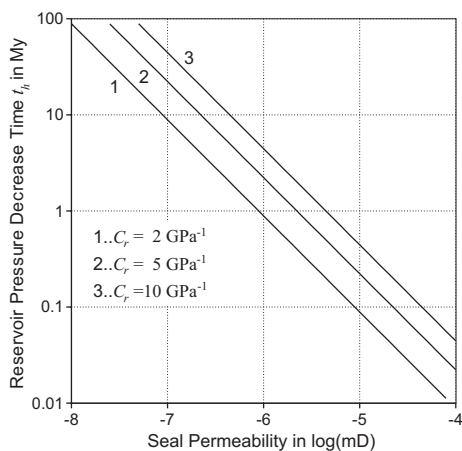


**Fig. 2.22.** Reservoir pressure decrease times  $t_h$  for various seal permeabilities  $k_s$  and  $h_r = 200$  m,  $h_s = 200$  m,  $\nu = 0.5$  mPa s



hydrostatic state, pressure increases in impermeable layers, and large overpressure areas occur below low permeability seals. Additionally, high permeable layers transmit high water flow rates and yield overpressure equalization in the layer. Even thin high permeable layers affect the multidimensional overpressure field, especially when they are expanded over long distances or large depths. This is illustrated in Fig. 2.23, where high permeability sand layers of very different depths are well connected to each other and yield almost the same overpressure everywhere in the sands. The calculated difference for the connected layers with a permeability of  $k = -2.5 \times \log(\text{mD}) = 3.2 \times 10^{-3}$  mD is about  $\Delta u = 0.01$  MPa.

The pressure difference is higher, when low permeability rocks interrupt the connectivity of the sands. Darcy's law states, that the assumption of the same overall flow rate results in an increase in the pressure difference by one order of magnitude, when the connected permeability decreases by one order of magnitude (10 mD). This example shows how sensitive the multidimensional pressure solution depends on the connectivity of the highly permeable facies.

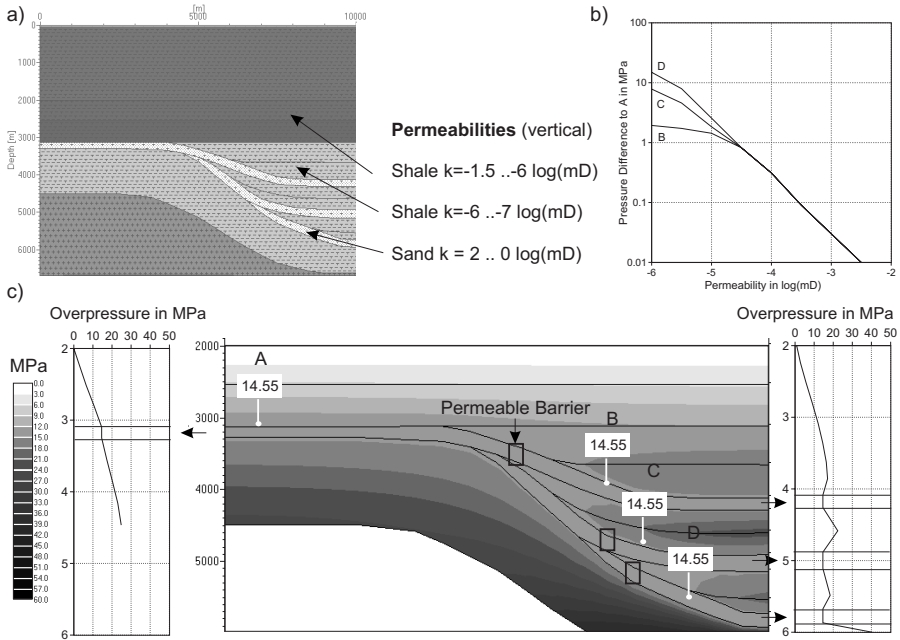


**Fig. 2.23.** Overpressure equalization along high permeability layers: (a) connected highly permeable sand layers are embedded in a thick shale package and yield almost the same overpressure in the three sandy sub-layers. (b) The pressure difference in the sand layers is almost proportional to the log permeability of the barrier. (c) Pressure solution with highly permeable barriers between the sands

Another similar example is shown in Fig. 2.24. Here a permeable layer connects a highly overpressured area below a thick shale block with a shallow hydrostatic pressure area. This permeable layer is able to discharge the pressure below the shale with resting pressure gradients equivalent to the permeability values of the connecting layer. A 3D example (Fig. 2.25) with a thin permeable layer varying over several kilometers of depth, also shows the pressure equilibration effect along a highly permeable flow avenue. These examples show how the architecture of the sediments in the basin control the pressure distribution.

The overpressure equation (2.13) does not deliver a solution in impermeable facies, such as salt, granite, or basalt, since these permeabilities are equal to zero. The pressure in impermeable structures should be equal to lithostatic pressure, since any fluid inclusion enclosed in an impermeable environment could never drop its pressure due to fluid outflow and must bear the total overburden. Hence, the inner points of impermeable rocks and salt are set as inner boundary conditions with values equal to the lithostatic potential. The overpressure gradient at the top of a salt dome can be a multiple of the lithostatic gradient as the overpressure can increase from a nearly hydrostatic

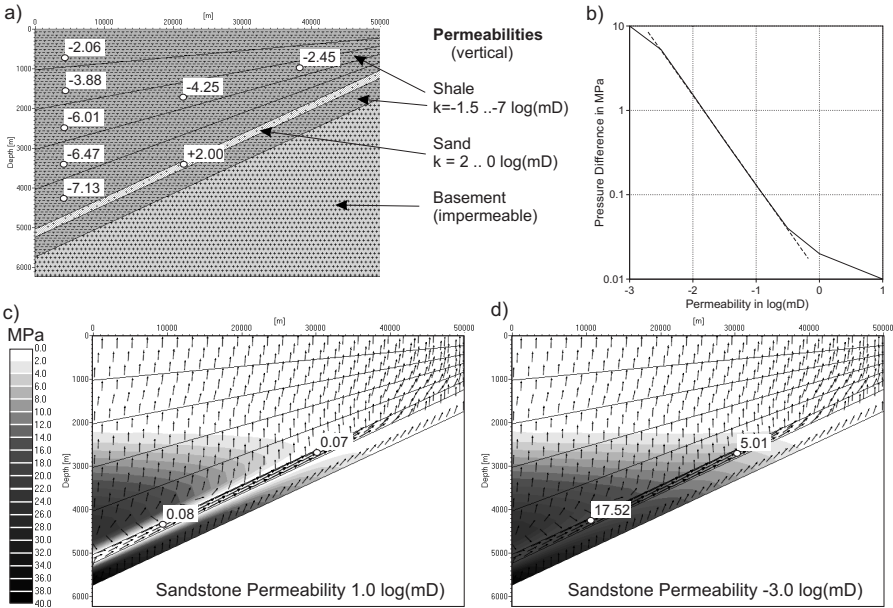


**Fig. 2.24.** Overpressure discharge in a highly permeable layer: (a) the highly permeable layer connects a high pressure area with a hydrostatic exit. (b) The pressure gradient in the sand layer gradually decreases with increasing permeability. (c), (d) 2D-overpressure fields for two different permeabilities of the permeable layer

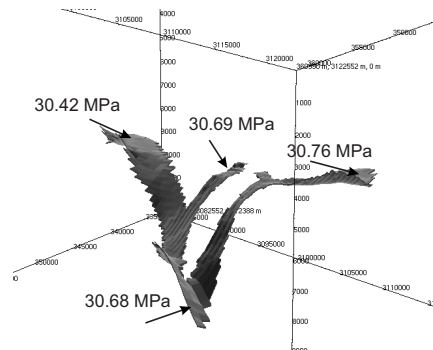


**Fig. 2.25.** Small overpressure differences along a 100 m thin layer with a permeability of  $k = 10^{-2}$  mD

regime in the sediments above to a lithostatic regime in the salt layer over a very short distance.

Uplift, together with erosion, yields overpressure release, since overburden load is decreased, but the porosity is almost maintained and the decompaction path during uplift is different from the normal compaction line (Fig. 2.6). Hence, the compressibility during uplift is much smaller (or close to zero),



which results in lower pressure release during erosion when compared with pressure formation during burial.

Some of the multidimensional pressure effects are illustrated in the example calculation of a 2D cross section from the Santos basin offshore Brazil (Fig. 2.26). The pressure is hydrostatic in the shallow area up to the top overpressure surface in 1 to 3 km depth. The pressure is lithostatic in the impermeable salt domes. High overpressure occurs below the thick salt domes, which gradually decrease toward the salt window. The overpressure is much lower below the smaller salt bodies. A thick block of low permeable shale layers also causes overpressure formation, while overpressures are almost equilibrated in the highly permeable facies.

In the above description, the upper pressure boundary condition at the sediment-water-interface is set to zero overpressure. In areas above sea level, the upper boundary is the groundwater surface and the pressure boundary condition is the groundwater potential, which is equal to the weight of the groundwater column above sea level. The pressure variable  $u$  in equation (2.13) is named hydraulic potential instead of overpressure in the terminology of groundwater specialists. Both terms are synonymous. The onshore groundwater level far from the coast is usually only some meters beneath the surface. The topographic surface can be taken as the approximate groundwater surface. The groundwater level close to the coast, or in very steep mountains can be significantly decreased, so that the boundary value of the corresponding hydraulic potential must be applied nearer to sea level with a much lower value.

An onshore example with a groundwater potential is shown in Fig. 2.27. The model has an aquifer with a depth of 3 km and a water flow towards the hydrostatic zone. The resulting water flow system and overpressure field of the basin is a superposition of three effects: the topographic driven flow near the surface follows the surface profile, the sedimentation controlled overpressure flow is directed out of the thick sediments, and the aquifer layer transports water toward the hydrostatic area. The water flow is much faster and the overpressure is much smaller, when the mountains are less extended as shown in Fig. 2.27.c.

The formation of mountains is always related with uplift and erosion, which is accompanied by a decrease in the overpressure potential of the uplifted blocks, since overburden is released during erosion. The overpressure release in rapid uplift and erosional periods below the mountains can be so high, that under-pressures arise in the aquifers, and the water flow can redirect toward the mountains as shown in Fig. 2.27.d. An analytical solution of a linearly varying horizontal groundwater potential is described in App. C.

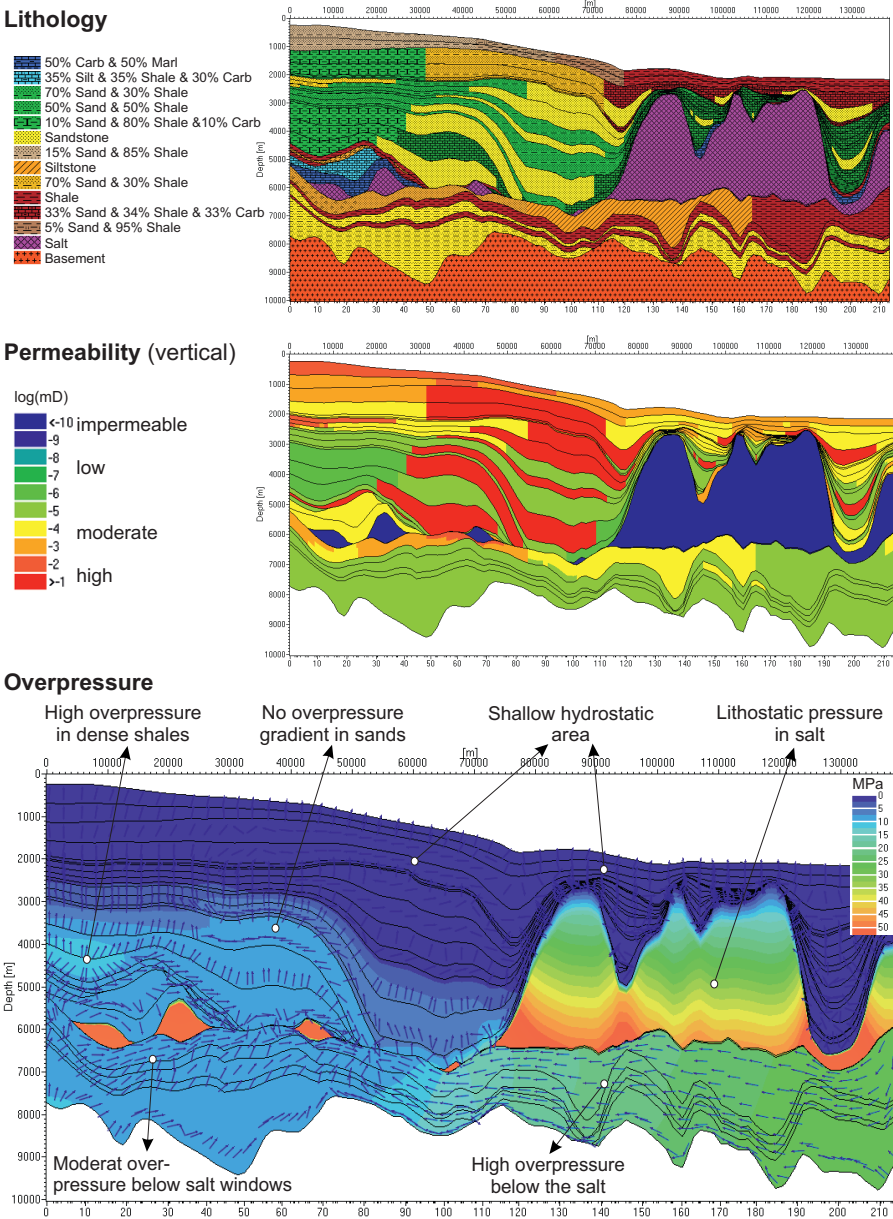


**Fig. 2.26.** Overpressure formation along a 2D cross section in the Santos basin, Brazil. The blue vectors indicate water flow

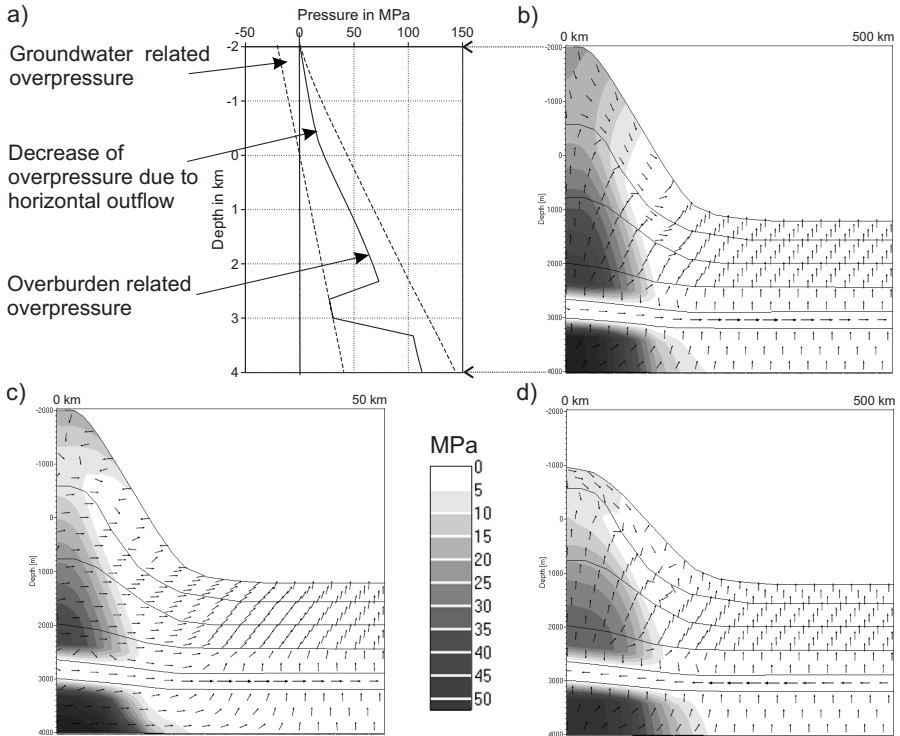


**Fig. 2.27.** Overpressure formation in an schematic onshore model: (a) 1D-extractions of pressures along a well with an aquifer at 3 km depth. (b) Overpressure formation and water flow vectors at present day. (c) Effect of mountain width, the model length is one tenth compared to model (b). (d) Effect of erosion: uplift is linked with erosion. The water flow vectors in the aquifer change direction from left to right

## 2.3 Special Processes of Pressure Formation

Special processes of pressure formation are quartz cementation (chemical compaction), aquathermal pressuring, pressure formation due to petroleum generation and cracking, and mineral transformations such as smectite–illite or gypsum–anhydrite.

### 2.3.1 Chemical Compaction

All sandstones and carbonates are cemented during burial. Quantitative descriptions of cementation processes are proposed by several authors (Walderhaug, 1996, 2000; Walderhaug et al., 2001; Bjørkum, 1996; Bjørkum and Nadeau, 1998; Bjørkum et al., 1998, 2001; Schneider et al., 1996; Schneider and

Hay, 2001; Lander and Walderhaug, 1999). Quartz cementation can be regarded as a three step process: quartz dissolution at grain-grain contacts, transport of the dissolved silica through pore space and precipitation of silica on free quartz grain surfaces (Walderhaug 1996, Figs. 2.28, 2.29). The transport of the solutes is performed via diffusion or pore water flow. All three processes (dissolution, solute transport and precipitation) have different effects on compaction, porosity reduction and pore pressure change. The cementation rate is controlled by the subsurface conditions, the water flow and water chemistry. Subsurface conditions are temperature, total vertical stress, and pore pressure. Water flow rates depend on the permeabilities of adjacent rock, and water chemistry is characterized by the dissolved minerals and the pH-value. It is a common approach to reduce the model to the precipitation process and assume that the other processes always supply enough silica.

**Fig. 2.28.** Principal processes of chemical compaction: (A) Pressure dissolution of silica into pore water. (B) Diffusion of dissolved silica within the pore water phase. (C) Precipitation of silica at quartz grains

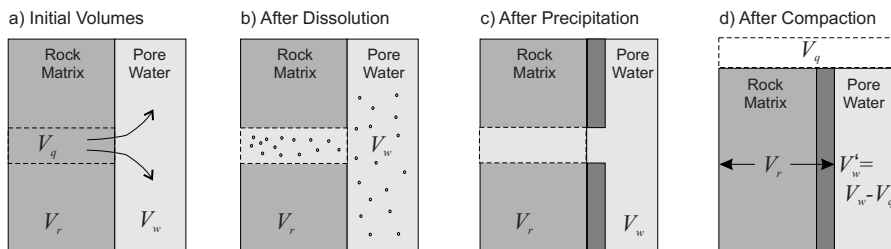
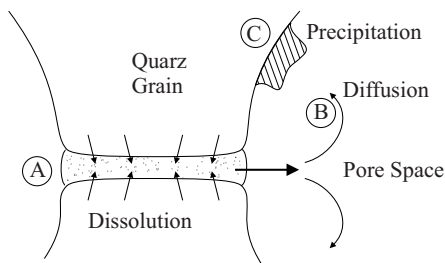


**Fig. 2.29.** Schematic volume balance for quartz dissolution and precipitation

The volume balance includes changes in the the solid volume (including cement)  $V_s$ , the pore fluid volume  $V_w$ , the volume of the precipitated cement  $V_q$ , and the total volume  $V_t = V_s + V_w$  with the porosity  $\phi = V_w/V_t$  and the cementation  $\psi = V_q/V_t$ .

Dissolution of silica occurs along the grain contacts. The contact zone is a thin film of adsorbed fluids between the rough surface of quartz grains. The dissolution rate  $C_d$  is mainly controlled by the effective stress (pressure dissolution) and is dependent on temperature.

$$C_d(\sigma'_z, T) = -\frac{1}{V_t} \frac{\partial V_s}{\partial t} . \quad (2.53)$$

During dissolution, the solid rock volume is decreased by the amounts of dissolved quartz, while the pore volume is increased by the same amount.

The dissolved silica is transported in water by diffusion and together with water as a separate phase flow. Hence, it depends on the quartz solubility of water, the diffusion rate, the permeabilities and overpressure gradients. The literature distinguishes between an open and closed systems approach, assuming relatively long and short transport paths (Schneider et al., 1996). The closed systems approach is more important, since quartz is usually precipitated near to the location of dissolution. However, the transport of dissolved silica does not influence the porosity, compaction and overpressure. Precipitation of silica as cement occurs on the free grain surfaces with preference to pore throats, which decreases permeability significantly. Precipitation rates  $C_p$  are usually temperature dependent (Walderhaug, 1996).

$$C_p(T) = \frac{1}{V_t} \frac{\partial V_s}{\partial t} . \quad (2.54)$$

Pure precipitation increases the amount of solid material and reduces the pore space by the same amount. The total balance of quartz dissolution and precipitation is as follows.

$$\frac{\partial V_s}{\partial t} = (C_p - C_d) V, \quad \frac{\partial \psi}{\partial t} = C_p . \quad (2.55)$$

The total process yields much lower porosities for high effective stresses than pure mechanical compaction would allow. It also increases the pore pressure, since the dissolution of the solid matrix transfers lithostatic pressure to pore pressure.

### Closed System Approach

In the closed system approach, short diffusion tracks are assumed with precipitation near to the locations of dissolution. Hence, the precipitation rate is equal to the dissolution rate and the total solid volume remains constant. The ability to drop the porosity by cementation additionally to mechanical compaction requires a change in the compaction law by either increasing the bulk compressibility or adding an additional term  $f_c$  as follows.

$$\frac{\partial \phi}{\partial t} = -C \frac{\partial \sigma'}{\partial t} - f_c(T, \sigma') \quad (2.56)$$

with the Terzaghi's compressibility  $C$  for mechanical compaction.

The cementation controlled porosity loss is also realized by accompanied water outflow and it is usually almost equal to the relative volume of the

precipitated cement ( $f_c \approx \partial\psi/\partial t$ ). The measured relative volumes of silican cement  $\psi$  are often used to derive empirical rules for the compaction term  $f_c$ .

Empirical laws for the cementation rate are proposed by Walderhaug (2000) and Schneider et al. (1996), named respectively the Walderhaug and Schneider models. The Walderhaug model is a precipitation rate-limited reaction controlled by the temperature and the quartz surface area available for precipitation. Walderhaug argues, that there is usually enough effective stress at large depth to supply enough dissolved quartz and that the effective stress dependency of the chemical compaction can be neglected. He proposed the following relationship with an Arrhenius type temperature dependency:

$$\frac{\partial\phi}{\partial t} = -\frac{M_q}{\rho_q} \frac{6(1-f_q)f_v}{d_q} \frac{\phi}{\phi_0} A e^{-E/RT} \quad (2.57)$$

where  $R$  is the gas constant with  $R = 8.31447 \text{ Ws/mol/K}$ ,  $f_q$  is the quartz grain coating factor (the fraction of the quartz grain surface that is coated and unsuitable for precipitation),  $f_v$  is the quartz grain volume fraction when precipitation starts (the fraction of the detrital grains that are quartz),  $d_q$  is the average quartz grain size, and  $A$  and  $E$  are the frequency factor and activation energy of the quartz precipitation rate. Fixed parameters are  $M_q = 0.06009 \text{ kg/mol}$  and  $\rho_q = 2650 \text{ kg/m}^3$ , the quartz molar mass and density. Default parameters are  $f_q = 5$ ,  $f_v = 1$ ,  $d_q = 0.03 \text{ cm}$ ,  $A = 10^{-11} \text{ mol/cm}^2/\text{s}$ , and  $E = 61 \text{ kJ/mol}$ . The activation energy is primarily used for calibration, when sample data are available. The porosity loss described by the Walderhaug model is shown in Fig. 2.30 for various activation energies with smaller cementation rates for higher activation energies.

A viscoplastic type compaction model is proposed by Schneider et al. (1996), who introduced the porosity loss rate proportional to the effective stress  $\sigma'_z$ , which represents the quartz supply by pressure induced dissolution. The rate is dropped by a viscosity  $\mu$ , which decreases with higher temperature according to an Arrhenius type dependency.

$$\frac{\partial\phi}{\partial t} = -(1-\phi) \frac{\sigma'_z}{\mu}, \quad \mu = \mu_0 \exp \left[ \frac{E}{k} \left( \frac{1}{T} - \frac{1}{T_0} \right) \right] \quad (2.58)$$

with the reference temperature  $T_0 = 15^\circ\text{C}$  and viscosity  $\mu_0 = 50 \text{ GPa/My}$ . The activation energy  $E$  can be used for calibration with default values between 16 and 18 kJ/mol. Porosity loss curves for fast and slow sedimentation are shown in Fig. 2.31 for various activation energies. Contrary to the Walderhaug model, porosity rates increase with higher activation energies.

The additional term in the compaction law also appears in the revised pressure equation according to (2.11) as follows:

$$C \frac{\partial u}{\partial t} - \nabla \cdot \frac{\mathbf{k}}{\nu} \cdot \nabla u = C \frac{\partial u_l}{\partial t} + f_c(\sigma'_z, T). \quad (2.59)$$

The increase in pressure is caused by the transfer of rock stress to pore pressure due to the abbreviation of the vertical stress bearing rock elements, by the

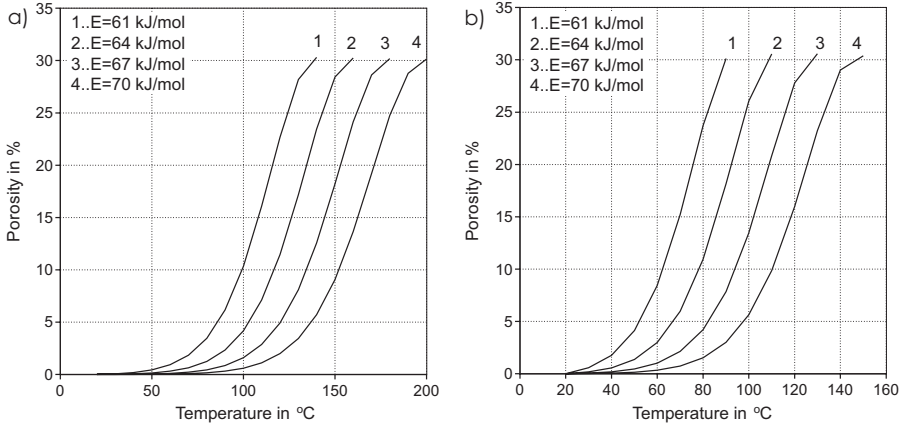


**Fig. 2.30.** Cemented porosity calculated with the Walderhaug model with coating factor  $f_q = 0.5$ , quartz grain volume fraction  $f = 1$ , quartz grain size  $d_q = 0.3 \text{ mm}$ , initial porosity  $\phi_0 = 41 \%$ , frequency factor  $A = 10^{-11} \text{ mol/cm}^2/\text{s}$ : (a) with high sedimentation rates  $S = 1.0 \text{ km/My}$ , (b) with low sedimentation rates  $S = 0.1 \text{ km/My}$

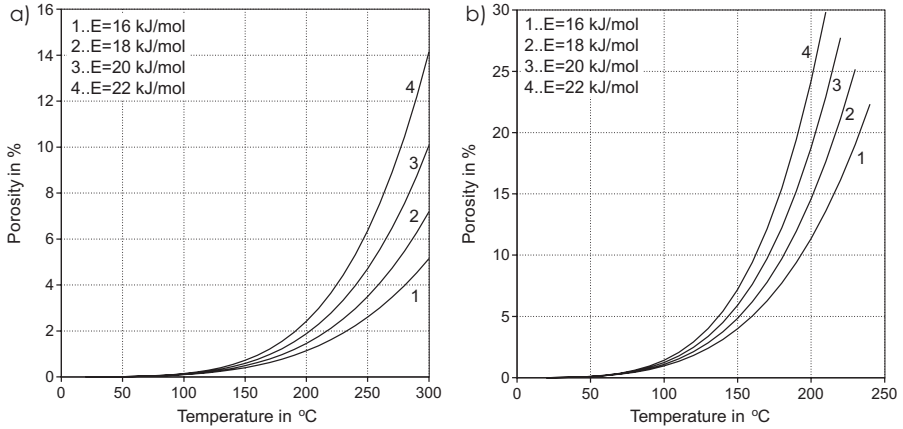


**Fig. 2.31.** Cemented porosity calculated with the Schneider model with a temperature gradient  $dT/dz = 30^\circ\text{C/km}$ , effective stress gradient  $d\sigma'_z/dz = 10 \text{ MPa/km}$ : for sedimentation rates (a)  $S = 0.1 \text{ km/My}$ , (b)  $S = 1 \text{ km/My}$

pore space reduction due to precipitated cement, and by the permeability decrease due to thinner pore throats.

An one dimensional example is shown in Fig. 2.32 with alternating shale and sandstone layers. The Walderhaug and Schneider models are compared with respect to porosity loss and additional overpressure generation. The Walderhaug model generally predicts higher cementation rates than the Schneider model. The difference in porosity loss (Fig. 2.32) is very high when the proposed default values are used. The effects are more similar when higher activation energies, rather than the default values, are used in both models. Cementation of the sandy layers yields lower permeability values which significantly influence the dewatering of the shale layers below. Additional overpressures in the sandstones also influence the pressure formation and porosity loss of the overlaying shales.

### 2.3.2 Fluid Expansion Models

Fluid expansions yield fluid density increases and related overpressure formation, which can be described with an additional source term  $f_a$  in the overpressure equation (2.59) as follows:

$$C \frac{\partial u}{\partial t} - \nabla \cdot \frac{\mathbf{k}}{\nu} \cdot \nabla u = C \frac{\partial u_l}{\partial t} + f_c(\sigma'_z, T) + f_a(T) . \quad (2.60)$$

The source terms in the above equation are understood as the relative pore fluid volume increase over time. The volumetric formulation is obtained, as in the initial mass balance equation (2.10) all the terms were already divided by the pore water density assuming that the water density variations with depth and time are relatively small on the considered scale. The fluid expansion models are here formulated on volume and not on mass balances, although variable fluid densities are considered. They are easier to implement and overview and the differences to more complex formulations are of minor importance (Luo and Vasseur, 1992, 1996). One can also integrate the source terms over the entire burial history for a deep sediment, for example in 5 km depth, to compare the order magnitudes of the different sources for pressure formation with each other. The total source for overburden load  $F_o$  is:

$$F_o = \int_t C \frac{\partial u_l}{\partial t} dt \approx \bar{C} \bar{u}_l \approx 0.75 \quad (2.61)$$

where  $\bar{C} \approx 10 \text{ GPa}^{-1}$  is the average bulk compressibility and  $\bar{u}_l \approx 75 \text{ MPa}$  is an average total load of a sediment in 5 km depth. Assuming, that in the initial sedimentation phase approximately one third of the overburden was not converted to overpressure, a value of 0.5 is more realistic.

The total load source for chemical compaction  $F_c$  is equal to the total porosity reduction  $\Delta\phi$  by cementation:

$$F_c = \int_t \frac{\partial \phi}{\partial t} dt \approx \Delta\phi \approx 0.15 . \quad (2.62)$$



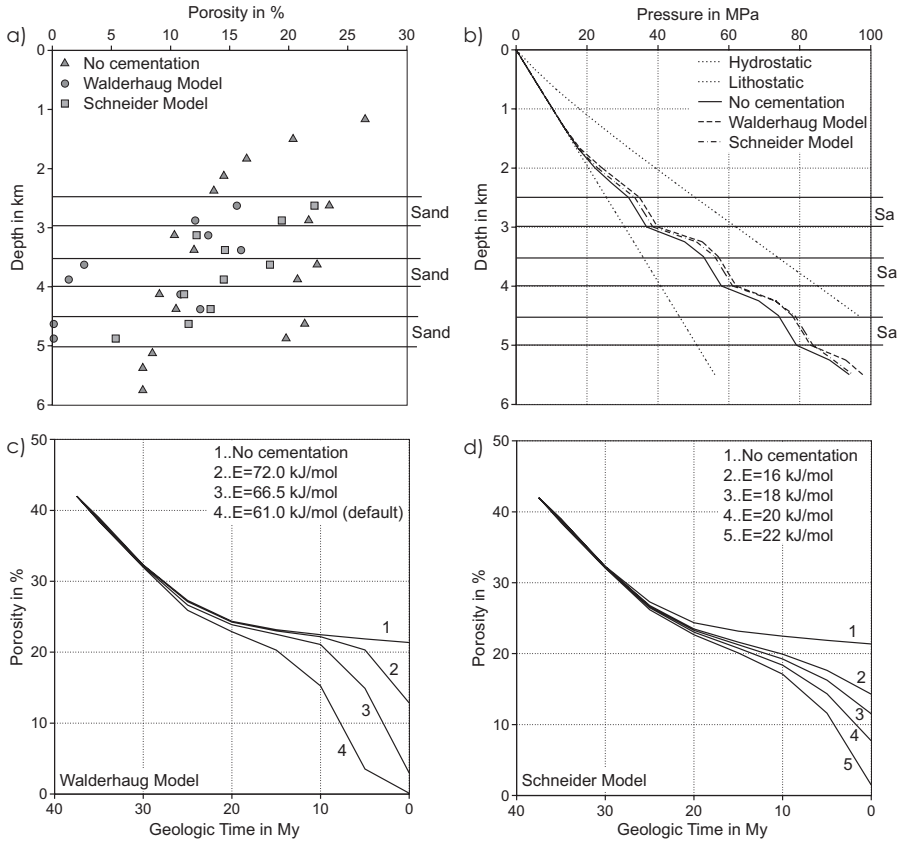


**Fig. 2.32.** 1D example of three sandstone layers embedded in shale depositions. Porosity loss and overpressure formation is calculated with the Walderhaug and Schneider model for cementation of the sandstone layers and without cementation for comparison. (a) Porosity loss due to mechanical and chemical compaction. The activation energies of the Walderhaug and Schneider model are 61 kJ/mol and 20 kJ/mol. (b) Overpressure formation during cementation. (c), (d) Porosity loss of the lower sandstone layer calculated with the Walderhaug and Schneider model, respectively, for different activation energies

This has a significant effect compared to the overburden load, but is locally restricted to sandstone and carbonate layers only.

### Aquathermal Pressuring

Luo and Vasseur (1992) investigated the effect of overpressure formation caused by thermal expansion of the pore water. The additional source term  $f_a$  in the overpressure equation depends on the isobaric thermal expansion coefficient  $\alpha = \alpha_w - \alpha_r$ , which is the difference between the values for water

$\alpha_w = 5 \times 10^{-4} \text{ K}$  and rock  $\alpha_r = 3.3 \times 10^{-5} \text{ K}$ .

$$f_a = \alpha \frac{\partial T}{\partial t} \quad (2.63)$$

which yields the following estimation for the total load source:

$$F_a = \int_t \alpha \frac{\partial T}{\partial t} dt \approx \Delta\phi \approx 0.07 \quad (2.64)$$

with an assumed temperature  $T = 150^\circ\text{C}$  in a depth of 5 km. Assuming, the overburden is not converted to overpressure for early sedimentation, a value of 0.05 is more realistic. It is one order of magnitude smaller than the effect from the overburden load. The aquathermal pressure formation depends on the heating rate and it becomes higher for fast burial.

### Mineral Transformations

Some mineral transformations, such as smectite to illite and anhydrite to gypsum conversion are related to pore fluid volumes changes. The conversion from smectite to illite occurs in all shales and shaly rocks and is described as a complex multi-stage process (Pytte and Reynolds, 1989; Swarbrick et al., 2002). Some of the related processes increase and some decrease the pore water volume with a general release of bound water into pore space and with a total increase of the water relative volume up to 5%. The volume of the solid matrix is also generally increased, since mainly  $\text{Na}^+$  ions are exchanged by  $\text{K}^+$  ions with a higher ion radius. This process is controlled by temperature and the availability of  $\text{K}^+$  ions in the rock matrix. A widely accepted model was proposed by Pytte and Reynolds (1989) as a fifth-order reaction of the following type.

$$\frac{\partial x}{\partial t} = -x^5 k_1 k_2 \quad (2.65)$$

where  $x$  is the smectite to illite ratio with an initial value of 0.8,  $k_1 = 74.2 \exp(-2490/T[\text{K}])$  is the chemical activity of potassium to sodium and  $k_2 = 1.64 \times 10^{21} \text{ My}^{-1} \exp(-16600/T[\text{K}])$  is a Arrhenius type temperature dependence. The equation can be written as a usual unimolecular forward reaction type (Chap. 4) as follows:

$$\frac{\partial x}{\partial t} = -x^5 A e^{-E/RT} \quad (2.66)$$

with the activation energy  $E = 37.9 \text{ kcal/mol}$ , the frequency factor  $A = 1.217 \times 10^{23} \text{ My}^{-1}$  and the gas constant  $R = 8.31447 \text{ Ws/mol/K}$ . The conversion depends on the heating rate, which is controlled by sedimentation rates (Fig. 2.33). The simple approach is, that the transformation ratio of the reaction  $\text{TR}_s = (x - 0.2)/0.8$  is related with a constant factor  $\kappa \approx 0.05$  to the load source  $f_a$  as follows:

$$f_a = \kappa \frac{\partial}{\partial t} \text{TR} . \quad (2.67)$$

Hence, the overpressure formation caused by smectite to illite conversion also depends on the sedimentation rates with a total source of

$$F_a = \int_t \kappa \frac{\partial}{\partial t} \text{TR} dt = \kappa \approx 0.05 . \quad (2.68)$$

This effect is one order of magnitude smaller than the overburden load effect. Osborne and Swarbrick (1997) and Swarbrick et al. (2002) proposed the separate consideration of smectite dehydration with the release of interlayer water, but the authors consider this effect to be included in the usual mechanical compaction model for shale.

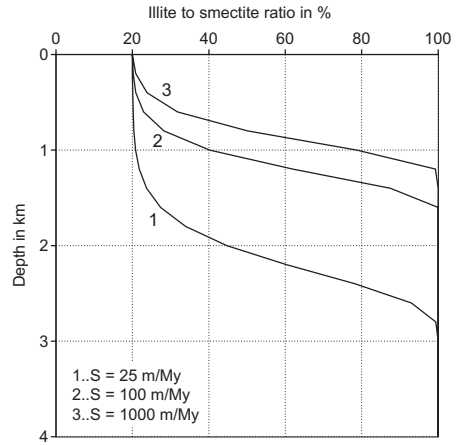


**Fig. 2.33.** Smectite–Illite after Pytte and Reynolds (1989) calculated for uniform sedimentation with different sedimentation rates

## Petroleum Generation Pressure

Catagenetic processes of organic matter change the relative volumes of kerogen, liquid, and vapor petroleum (Fig. 2.34). Here, the primary cracking of kerogen and secondary cracking of the heavier petroleum components are taken into account. The controlling parameters are the changes of the petroleum phase masses and volumes, which result from the generated chemical components and the PVT controlled dissolution into the two petroleum phases (Chaps. 4, 5). The fluid models also provide corresponding modifications of the phase densities, which control the generation driven overpressure formation. The actual densities (mass per volume) of the generated petroleum components, which are dissolved in liquid and vapor phase, are denoted as  $\mu_l$  and  $\mu_v$  with the phase densities  $\rho_l$  and  $\rho_v$ , respectively. Then, the load source for primary generation is as follows:

$$f_a = \left( \frac{1}{\rho_l} - \frac{1}{\rho_k} \right) \frac{\partial \mu_l}{\partial t} + \left( \frac{1}{\rho_v} - \frac{1}{\rho_k} \right) \frac{\partial \mu_v}{\partial t}. \quad (2.69)$$

The kerogen density  $\rho_k$  has to be taken into account, since the reduction of kerogen volume during cracking is also a significant value. For the estimation of the magnitude of the load source, all generated petroleum with mass density  $\mu_p$  is assumed to be dissolved in one super-critical petroleum phase with density  $\rho_p$ . It follows from (4.8):

$$F_a = \int_t \left( \frac{1}{\rho_p} - \frac{1}{\rho_k} \right) \frac{\partial \mu_p}{\partial t} dt \approx \left( \frac{\rho_r}{\rho_p} - \frac{\rho_r}{\rho_k} \right) \text{TOC}_0 \text{HI}_0 (1 - \phi) \approx 0.033 \quad (2.70)$$

with an initial total organic carbon content  $\text{TOC}_0 = 5\%$ , an initial hydrogen index  $\text{HI}_0 = 500 \text{ mgHC/gTOC}$ , a porosity  $\phi = 20\%$ , and densities of  $\rho_k = 800 \text{ kg/m}^3$ ,  $\rho_p = 500 \text{ kg/m}^3$ ,  $\rho_r = 2200 \text{ kg/m}^3$ . This effect is one order of magnitude smaller than the overburden load effect and it is restricted to source rocks only. Exceptions are coals with TOC values higher than 50 % and coal bed methane production, which can form very high overpressures in place. Gas has a much higher compressibility ( $100 \text{ GPa}^{-1}$ ) than the porous framework ( $10 \text{ GPa}^{-1}$ ), which yields a retarded overpressure drop by pore fluid outflow as described in equation (2.52), when high gas saturations occur. This slightly increases the effect of gas generation controlled overpressures.

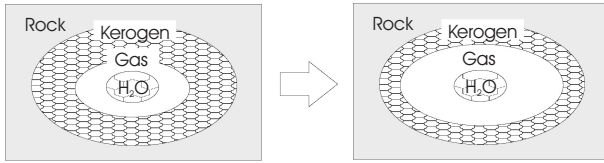


**Fig. 2.34.** Gas generation from kerogen changes the volumetrics of kerogen and pore fluids

Secondary cracking can also change phase volumes and can be described analogously to primary cracking. The resulting overpressure build up is much smaller, especially because coke with higher density is formed as a by-product.

The generation of petroleum amounts can be more accurately formulated in the multi-phase fluid flow equations (Chap. 2.9) with source terms for the generated masses. Luo and Vasseur (1996) published a detailed analysis for a two-phase system formulation with similar magnitudes for overpressure build-up as described in equation (2.70).

The overpressure equation with all described effects is as follows.

$$\begin{aligned}
C \frac{\partial u}{\partial t} - \nabla \cdot \frac{\mathbf{k}}{\nu} \cdot \nabla u &= C \frac{\partial u_l}{\partial t} + f_c(\sigma'_z, T) + \\
\alpha \frac{\partial T}{\partial t} + \kappa \frac{\partial \text{TR}}{\partial t} + \left( \frac{1}{\rho_l} - \frac{1}{\rho_k} \right) \frac{\partial \mu_l}{\partial t} - \left( \frac{1}{\rho_v} - \frac{1}{\rho_k} \right) \frac{\partial \mu_v}{\partial t} .
\end{aligned} \tag{2.71}$$

## 2.4 Overpressure Calibration

The overall overpressure is mainly determined by mechanical compaction. Other sources for overpressure, such as chemical compaction or fluid expansion, are often rather localized phenomena and for that reason not included in this section.

Mechanical compaction, as formulated in (2.13), relates pore water flow with porosity reduction and overpressure. An overpressure calibration is therefore a calibration of compressibility and permeability. It can be performed in two major steps. The first step deals with the adjustment of rock compressibilities and the second with permeabilities.

Compressibility is introduced via a relationship of effective stress and porosity in (2.17). Effective stress is defined as the difference  $\sigma' = \sigma - p\mathbf{I}$ . Relationship (2.17) describes a local property of the rock, and does not contain permeability. If porosity is known, a compaction model such as Athy's law or the Schneider model can be fitted to each lithology in the following way: porosity and pressure value pairs of the same lithology are collected for different depths and locations. It is possible to calculate the corresponding overburden from the basin model for these points. Thus, effective stress can be evaluated and plotted against porosity (Fig. 2.35). Finally, a compaction model with an effective stress versus porosity formulation, is fitted against these data points.

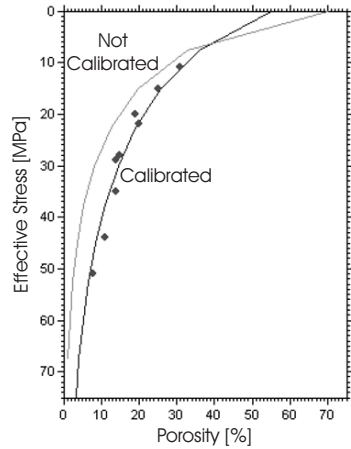
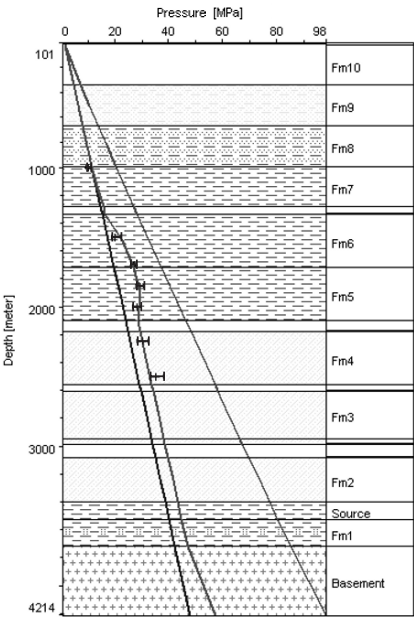


**Fig. 2.35.** Fit of Athy's law in porosity-effective stress formulation against a few data values

Note that this approach relates effective stress to porosity and not with depth. A porosity depth fit is not achieved until the second major calibration step of permeability adjustment is performed.

The second step consists of a permeability adjustment against overpressure. This step can be sophisticated because overpressure depends in general non-locally and ambiguously on permeability. For example, a pressure drop due to water outflow can often be modeled by different positions and sizes of the “leak”. However, some general rules of thumb can be stated. Highly impermeable rocks are not a matter for calibration. If there is no water flow within these rocks, a small change in permeability does not change the overpressure pattern at all. The situation is the other way around for highly permeable sand layers. A change in permeability will not change the overpressure pattern. It remains equilibrated inside these layers. Important for pressure calibration are the layers in which overpressure builds up or is released (Fig. 2.36). Obviously, a permeability variation for these rocks will cause a significant change in the overpressure pattern. Identification of these layers is a key point in overpressure calibration because it drastically reduces the number of calibration parameters.

**Fig. 2.36.** An example of a pressure calibration by adjustment of the permeabilities. Pressure builds up in layer Fm6 and is slightly released in layer Fm5. Hence Fm5 and Fm6 are the key layers in this example. It is possible to calibrate the model by variation of the permeabilities in these layers. Below Fm5 a highly permeable sandstone is located. It transports some water from this region through a slightly higher permeable window area in Fm5/Fm6, far away from this well. Hence it is necessary to incorporate and adjust the permeabilities in this window area for good calibration



Overpressure can, in principal, only be calibrated if the water flow and water balance is adjusted correctly throughout the entire basin. In practice this leads to a situation where the permeabilities of many layers, lithologies, and rock types must be adjusted simultaneously. Due to long range pressure inter-

actions caused by water flow, this is usually very problematic. It is found that it is possible to tackle the problem iteratively. Calibration is first performed on key layers which are connected directly or via other permeable layers to the top of the basin. Water is transported along these pathways out of the basin. Overpressure can be calibrated best if the total amount of water in the basin is adjusted first. According to this picture adjustments of permeabilities in more deeply buried regions will lead to a minor overall adjustment at least on the global water balance.<sup>1</sup> On average, the water flow is upward and therefore calibration should usually be performed from the top down and from more to less permeable lithologies. The procedure can be repeated iteratively until convergence is reached.

This workflow assumes, that recently no erosion with a reduction of overburden appeared. Otherwise, under the assumption of non-decompactable rocks, porosity must be fitted against the maximum effective stress. However, the maximum effective stress might not be calculable as necessary paleo overpressures are possibly unknown. This problem can be overcome with additional overpressure shifts at paleo times, which are also calibrated against the present day overpressure pattern. The whole overpressure calibration procedure including both steps must then iteratively be refined.

## 2.5 Geomechanical Models

The fundamentals of geomechanics would require a full book in itself. Here only the most important equations, which are needed for basin modeling, are mentioned. Detailed descriptions are given e.g. in Fjaer et al. (1992) and Parry (2004).

Solids conduct forces through the material and react with deformations. The forces and moments acting on each small volume element are described in terms of stress and the deformations are represented in terms of strains. Most materials respond with linear dependent recoverable strains on small stresses, which is called linear elasticity. In practice, stress–strain relations also have terms of non-linearity, irreversibly (plasticity), rate dependency (viscosity or creep) and yield failure, when certain limits of the stress components are exceeded.

The traditional stress–strain concept has been determined for solids. It can be extended to porous media with an introduction of effective stresses, which takes pore pressure into account. The difference between the concepts of rock and soil mechanics is that the first takes into account cement between the grains, while the second refers to unconsolidated rock with loosely connected grain particles.

---

<sup>1</sup> More deeply buried rocks are usually more compacted and therefore less permeable. This also reduces the capability of water transport and the range of influence on the overpressure pattern.

## 2.6 Stress and Deformation

The total bulk stress tensor is a superposition of the stress tensors of the grains and the pore pressure of the fluids. Tensors, their principal values and invariants are introduced in Sec. 8.2. The stress tensor  $\sigma_{ij}$  has normal ( $i = j$ ) and shear ( $i \neq j$ ) components, which act on surfaces perpendicular to the coordinate axes (Fig. 2.37). Compressional normal components are positive. The principal values are denoted as  $\sigma_1$ ,  $\sigma_2$ , and  $\sigma_3$  with  $\sigma_1 \geq \sigma_2 \geq \sigma_3$ . The boundary vector  $\mathbf{t} = \mathbf{n} \cdot \boldsymbol{\sigma}$  acting on arbitrary area with the normal  $\mathbf{n}$  has a normal and a tangential component  $t_n$  and  $t_t$ .

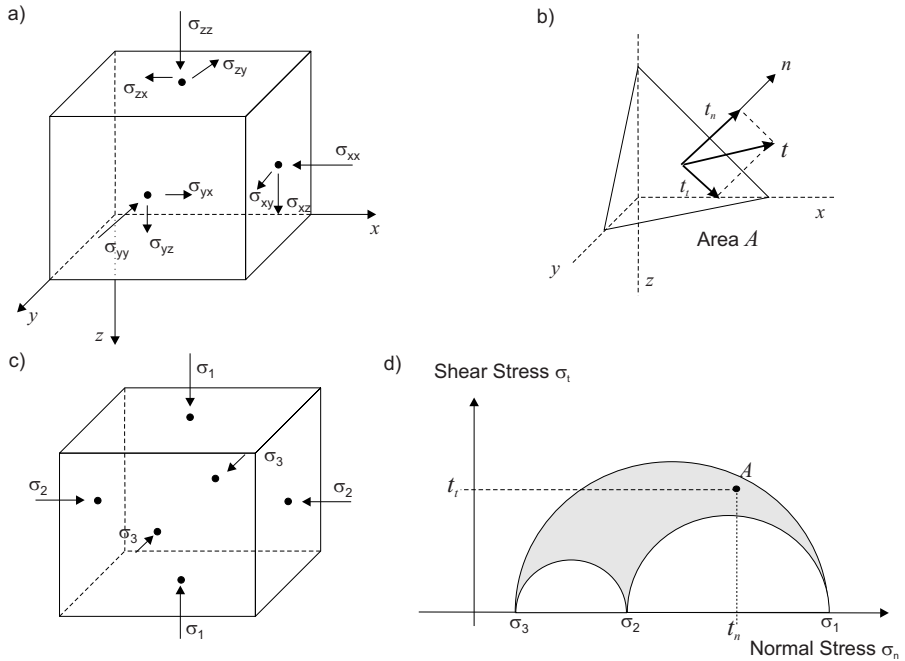


**Fig. 2.37.** Representations of the stress tensor. (a) Normal and shear components, (b) Boundary stresses at an arbitrary area, (c) Principal Stresses, (d) Mohr circles

There are two important representations of the three dimensional stress state: the Mohr circles used in rock mechanics and the “p-q” plots used in soil mechanics. The Mohr circle construction is based on principal stresses. An arbitrary 3D stress tensor is pictured with three circles (Fig. 2.37) in a normal-shear stress diagram and the area between the circles represents the boundary stress vector acting on any cut-plane of the volume element. The outer circle is important to analyze and illustrates rock failure. Stress in two dimensions is represented with only one circle. Mohr circles for the special cases of biaxial and isotropic stresses, and pure shear are illustrated in Fig. 2.38.



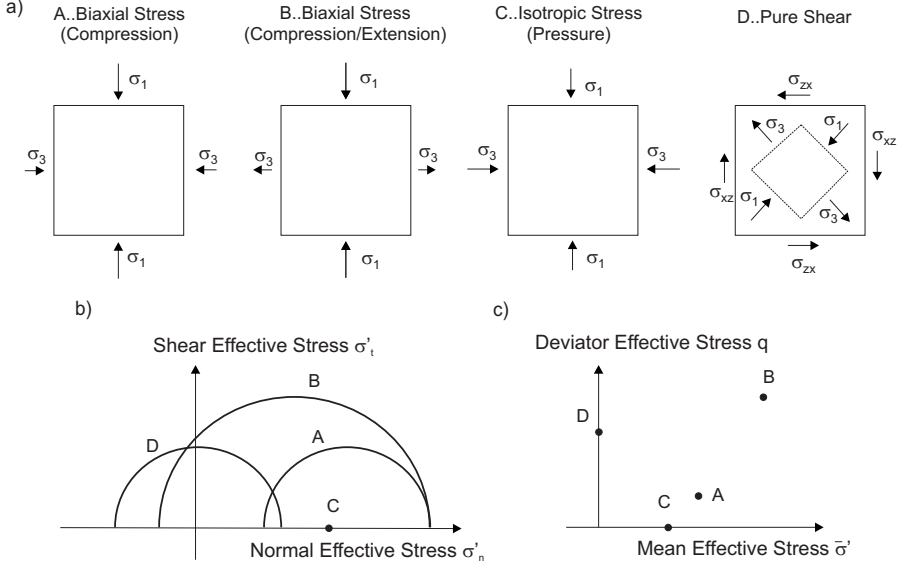


**Fig. 2.38.** Stress characterization of special load cases (a) Principal stresses for biaxial stresses, (b) Mohr circles, (c) soil mechanical p-q plot

The “p-q” plot uses two characteristic values, the mean stress  $\bar{\sigma}$  and the deviatoric stress  $q$ .<sup>2</sup> The mean stress is an average volumetric (compressional) stress and the deviatoric stress represents an average shear stress as follows:

$$\begin{aligned}\bar{\sigma} &= \sigma_1 + \sigma_2 + \sigma_3 \\ q &= \frac{1}{\sqrt{2}} [(\sigma_1 - \sigma_2)^2 + (\sigma_1 - \sigma_3)^2 + (\sigma_2 - \sigma_3)^2]^{1/2} .\end{aligned}\quad (2.72)$$

Any three dimensional stress state is a point in the “p-q” plot as illustrated in Fig. 2.38.

Any movement, rotation and deformation yields a change in the position of the sample particles, which is described with the displacement  $\mathbf{u}(\mathbf{r})$ . The deformation of a volume element is called strain  $\epsilon$  and can be derived from a given displacement vector as follows:

$$\epsilon = \frac{1}{2}(\nabla \mathbf{u} + (\nabla \mathbf{u})^T) . \quad (2.73)$$

This equation is only valid for small deformations. In case of large deformations, additional terms with products of  $\nabla u$  need to be incorporated in the above equation (Zienkiewicz, 1984). The strain tensor  $\epsilon_{ij}$  also has normal

<sup>2</sup> The symbol “p” is usually used in soil mechanics terminology instead of  $\bar{\sigma}$ , but the symbol “p” is already used for pore pressure here.

(or direct) ( $i = j$ ) and shear (or distortion) ( $i \neq j$ ) components. The total volumetric deformation  $\epsilon_v = 3\bar{\epsilon}$  is the sum of the principal strains:

$$\epsilon_v = \epsilon_1 + \epsilon_2 + \epsilon_3. \quad (2.74)$$

The two special deformations of pure and simple shear have no volumetric strain  $\epsilon_v = 0$  (Fig. 2.39).

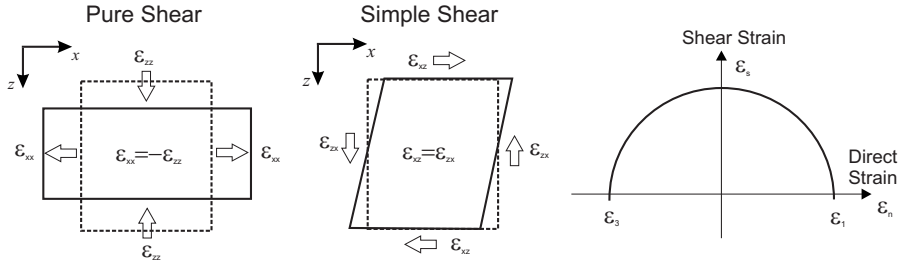


**Fig. 2.39.** Pure shear and simple shear are special deformations without volumetric strain. They are represented with the same Mohr circle, but they have different orientations of the axes

The elasticity tensor  $\mathbf{E}$  relates stresses and strains linearly  $\boldsymbol{\sigma} = \mathbf{E} \cdot \boldsymbol{\epsilon}$  assuming the linear theory of elasticity. It contains only two elastic parameters for isotropic behavior: the shear modulus  $G$  and the Poisson's ratio  $\nu$ .

$$\boldsymbol{\sigma} = 2G\boldsymbol{\epsilon} + \frac{2G\nu}{1-2\nu}\epsilon_v\mathbf{I} \quad (2.75)$$

where  $\mathbf{I}$  is the unit tensor. Alternatively, the Young's modulus  $E$  or the bulk modulus  $K$  can be used as follows.

$$E = 2G(1 + \nu), \quad K = \frac{2G(1 + \nu)}{3(1 - 2\nu)}. \quad (2.76)$$

Note, that the inverse of the bulk modulus is the bulk compressibility  $C = 1/K$ .

The meaning of the elasticity parameters is especially descriptive for uniaxial compression with  $\sigma_x$  and the two resulting strains  $\epsilon_x$  and  $\epsilon_y$ , where the elastic properties are  $E = \sigma_x/\epsilon_x$ ,  $\nu = -\epsilon_y/\epsilon_x$ , and  $K = \bar{\sigma}/\epsilon_v$ . Anisotropy is described with more than two elastic parameters in the elasticity tensor and non-linear elastic behavior with additional terms of higher order strains.

The principle of force equilibrium states, that any body force  $\mathbf{f}$  is compensated by the stress tensor.

$$\nabla \cdot \boldsymbol{\sigma} + \rho \mathbf{f} = 0 \quad (2.77)$$

where  $\rho$  is the bulk density. This yields the differential equation based boundary value problem for the model of linear elasticity (2.75) with the gravity (overburden) forces as follows.

$$G\Delta\mathbf{u} + \frac{G}{1-2\nu}\nabla\nabla\cdot\mathbf{u} + \rho g\mathbf{e}_z = 0. \quad (2.78)$$

The boundary values are displacements  $\mathbf{u}$  and boundary stresses  $\mathbf{t} = \mathbf{n} \cdot \boldsymbol{\sigma}$ . The differential equation is slightly different when large deformations are taken into account (Zienkiewicz, 1984).

The above theory of stresses and strains has been developed and proofed for pure solids. Extensions for composite media, as needed for pore fluids and rocks, require very complex models for pore pressure and rock stresses. There are simplified models proposed by Terzaghi on an experimental basis and Biot on theoretical derivations, both are based on the idea of introducing an effective stress  $\sigma'$  instead of the total stress  $\sigma$  and using the principal equations of the above concept with some modifications.

$$\boldsymbol{\sigma}' = \boldsymbol{\sigma} - \alpha p \mathbf{I}, \quad \text{with} \quad \alpha = 1 - \frac{K_b}{K_s} \quad (2.79)$$

where  $K_b$ ,  $K_s$  are the bulk moduli for the bulk framework and the solid rock matrix, respectively. Terzaghi's effective stress is defined for  $\alpha = 1$ , which is a good approximation except at very large depths. The corresponding effective stress based Mohr circles and "p'-q" plots for compacted sediments are illustrated and explained in Fig. 2.40.<sup>3</sup>

### 2.6.1 Failure Analysis

Elastic material response means, that characteristic stress values like  $\sigma_z$  or  $\bar{\sigma}$  increase linearly with the equivalent strain values  $\epsilon_z$ ,  $\epsilon_v$ . The corresponding stress-strain plots also show non-elastic behavior. The curves are usually obtained by rock mechanical laboratory measurements, such as drained and undrained uni- and triaxial tests. Mean stress and volumetric strain are the important parameters in basin modeling. Typical curves are shown in Fig. 2.41. Usually, elastic and elasto-plastic regions are distinguished, separated by the yield point, the point of maximum stress and the critical state point.

Elastic behavior means no permanent changes. Thus, the rebound curve is identical to the load curve. Beyond the yield point the specimen will not return to the original state, but it still supports increasing loads with yielding. Softening begins at the point of maximum stress. Further deformation yield less ability of the specimen to withstand stress. At the critical state, an instable deformation occurs, like rupture or pore collapse. Failure is usually defined at the point of maximum stress, although it is sometimes used for yielding, since the material structure changes.

<sup>3</sup> Equivalent to the term "p-q" plot, which was introduced as the mean stress versus deviatoric stress diagram, the "p'-q" plot depicts the mean effective versus the deviatoric effective stress diagram. Note that the deviatoric effective stress is equal to the deviatoric total stress for Terzaghi's definition of the effective stress (2.2).

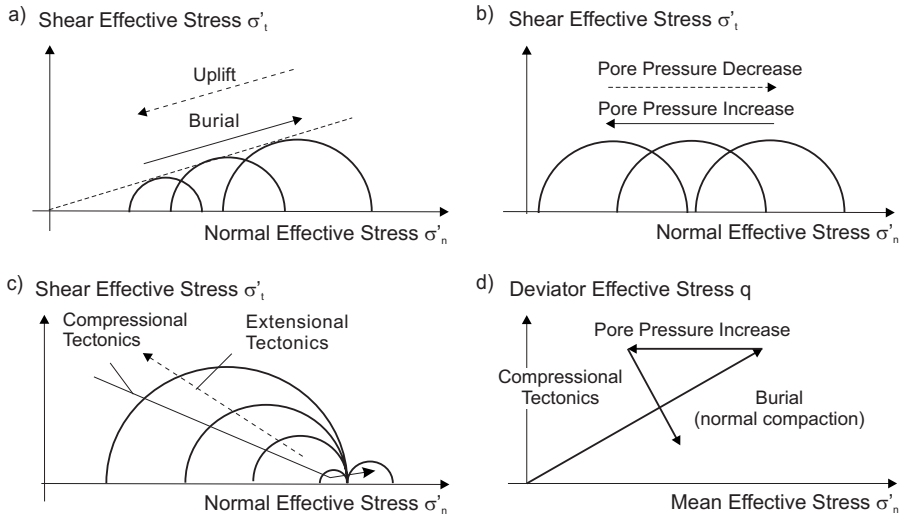


**Fig. 2.40.** Effective stress based Mohr circles and "p'-q" plots for (a) burial and uplift, (b) pore pressure changes, (c) tectonics. (d) Equivalent "p'-q" plot

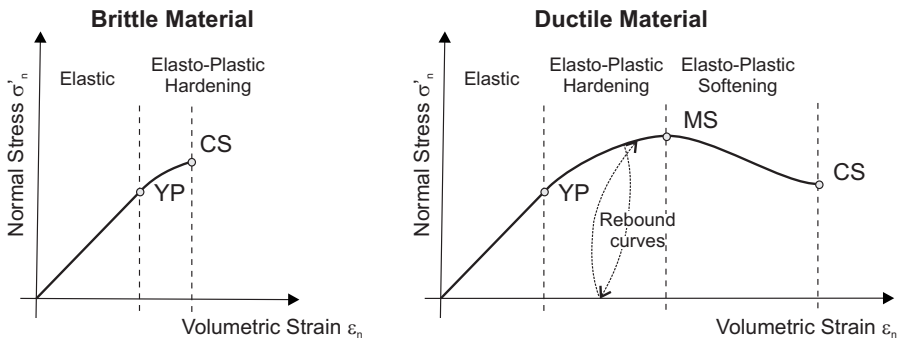


**Fig. 2.41.** Schematic stress versus strain plot for rocks. Characteristic points are the yield point (YP), the maximum stress point (MS) and the critical state point (CS). Brittle and ductile materials are distinguished by the relative length of the elasto-plastic region. The rebound curve has approximately the same steep angle as the linear elastic curve with a small hysteresis

The behavior of a sample is called ductile or brittle, when the elasto-plastic region is large or small. The curve in the elasto-plastic region of the same sample strongly depends on temperature and the speed of deformation.

## Mohr Type Failure

For an arbitrary three dimensional stress state, the failure criterion is a function of all principal stresses, the yield function  $f$ :

$$f(\sigma_1, \sigma_2, \sigma_3) = 0. \quad (2.80)$$

Mohr proposed a function, which depends only on maximum and minimum principal stresses. This is equivalent to a curve in the Mohr diagram (Fig. 2.42). Failure occurs when the Mohr circle intersects the failure line. The often used Mohr failure curve is a straight line with cohesion  $C$  and internal friction  $\mu$  as offset and steep angle of the line, respectively, which is called a Mohr–Coulomb failure.

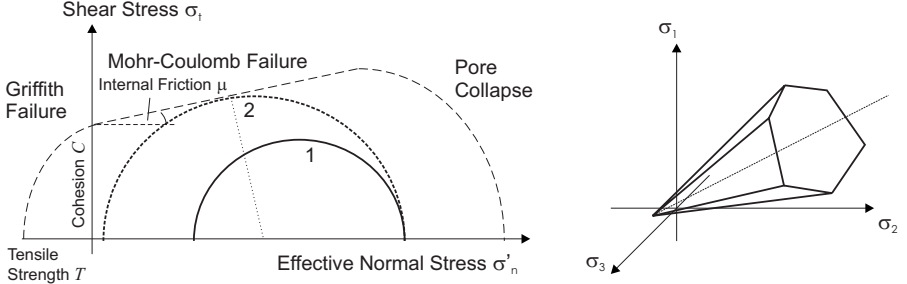


Fig. 2.42. Stresses and pressures in porous rocks

$$\sigma_t = C + \mu \sigma_n. \quad (2.81)$$

Mohr–Coulomb failure initiates plastic flow along a failure plane, which is directed at an angle  $\beta = (\pi + 2\mu)/4$  between the axes of  $\sigma_3$  and  $\sigma_1$ . The Mohr–Coulomb failure criterion is also equivalent to the surface of a hexagonal pyramid in the principal stress space (Fig. 2.42). A Mohr-type failure curve can also be used to describe pore collapse, but with a negative friction angle, which is equivalent to the “cap” of the Mohr–Coulomb pyramid.

In the extensional region, a Griffith type criterion is usually taken into account. It is derived from a microscopic theory of crack extension in two-dimensional samples. A simple generalization to three dimensional rock samples can be made with a parabolic failure curve in the Mohr diagram (Fig. 2.42), which is equivalent to a parabolic “top” in the principal stress space. Griffith formulated the failure equation for 2D only. The simplest extension to 3D-phenomena is Murell’s extension, where the failure surface, in terms of principal stresses, is also a parabolic surface with a simple pyramid on top.

$$\begin{aligned} (\sigma_1 - \sigma_3)^2 + (\sigma_1 - \sigma_2)^2 + (\sigma_2 - \sigma_3)^2 &= 24 T_0 (\sigma_1 + \sigma_2 + \sigma_3) \\ \text{or } \sigma_1 &= -T_0 \quad \text{or } \sigma_2 = -T_0 \quad \text{or } \sigma_3 = -T_0. \end{aligned} \quad (2.82)$$

Note, that the maximum tensile strength is the only failure parameter for Griffith failure and it is related to cohesion as  $C = 12 T_0$ . Griffith failure

can also be extended to compressional regions with the same formula. This is usually used for the description of fracturing as explained in Sec. 2.6.1.

### Plastic Flow and Critical State

The term critical state indicates damage and the inability of the specimen to support stresses. Usually, the same type of failure condition is used as for yielding, but with different material parameters  $C_0$ ,  $T_0$  and  $\mu$ . Plastic flow occurs from the onset of yielding until the critical state is reached. Then, the strain consists of elastic and plastic parts (Fig. 2.43),

$$\epsilon = \epsilon_e + \epsilon_p . \quad (2.83)$$

The elastic strain is still related to the effective stress tensor with the elastic modules, and the plastic deformations are directed perpendicular to the failure surface in the principal stress space.

$$d\epsilon_{p,ij} = d\lambda \frac{\partial f}{\partial \sigma'_{ij}} \quad (2.84)$$

where  $\lambda$  is the hardening parameter. In the above equation the plastic flow vector  $d\epsilon_{p,ij}$  is directed perpendicular to the yield surface in the  $\sigma$ -space. In porous media, a constant angle between flow vector and yield surface is usually assumed. In general, the function  $f$  can be different from the yield function and it is then called plastic potential. It is very important, to note, that the direction of the plastic flow is controlled by the failure parameters  $C_0$ ,  $T_0$  and  $\mu$ . Fault planes are directed along fixed angles between the minimum and maximum principal stresses. The formulation of the corresponding elasto-plastic boundary problem takes into account the plastic hardening law (2.84) and the yield condition (2.81). Detailed descriptions are given in Zienkiewicz (1984).

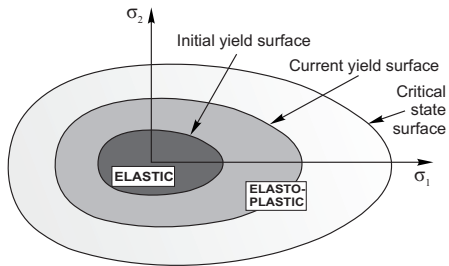
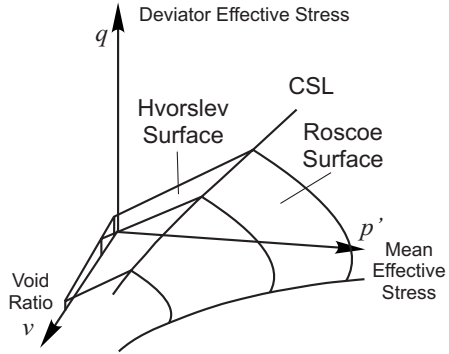


**Fig. 2.43.** Failure surfaces for yielding and critical state after Fjaer et al. (1992). The process of yielding is equivalent to hardening until the critical state is reached and damage occurs

The soil mechanical equivalent of the yield surface is the Roscoe and Hvorslev surface in the “p–q–v” diagram (Fig. 2.44), for normally consolidated

and overconsolidated rocks, respectively.<sup>4</sup> When the effective stress state in a rock intersects the yield surfaces, further compaction with increasing effective stress occurs along both failure surfaces until the critical state line.

**Fig. 2.44.** Failure surfaces in a soil mechanics “p’-q-v” diagram. When the compaction controlled effective stress paths hits the failure surface, further compaction follows the failure surfaces until the critical state line (CSL)



## Fracturing

Fracturing is another type of failure, which is the formation and growth of microfractures in rocks. Most fracture models are based on the Griffith theory, which defines a brittle failure surface in principal effective stress diagrams.

The most common type of fractures are tensile fractures. They are formed when traction exceeds the tensile strength  $T_0$ . Following the usual convention, traction is negative stress. Hence the maximum traction is equal to the minimum principal effective stress  $\sigma'_3$  and the condition for the initiation of fractures is

$$\sigma_3 - p = T_0 . \quad (2.85)$$

Obviously, the above condition is valid when the Mohr circle contacts the failure line on the left side (Fig. 2.42). The Mohr circle moves to the left mainly by overpressuring. The minimum overpressure, which is needed to initiate fracturing for a given stress state, is called the fracturing pressure. The fracturing pressure can be drawn in the pressure–depth space to illustrate the threshold pore pressure for fracturing (Fig. 2.42). It is a very common simplification in basin modeling programs to describe the fracturing condition with a fixed fracturing pressure versus depth curve (Fig. 2.45). The tensile strength differs for the different rock types. Hilgers et al. (2006) reported  $T_0 = 10$  MPa for sandstone and a significant smaller value for shale. Thus, the fracturing pressure gradient alternates within a shale–sand sequence.

Fracturing increases the rock permeabilities and drops the capillary entry pressures as described with the following relationship.

<sup>4</sup> Normally consolidated rocks are under the maximum effective stress, while overconsolidated rocks have a lower effective stress than at maximum burial

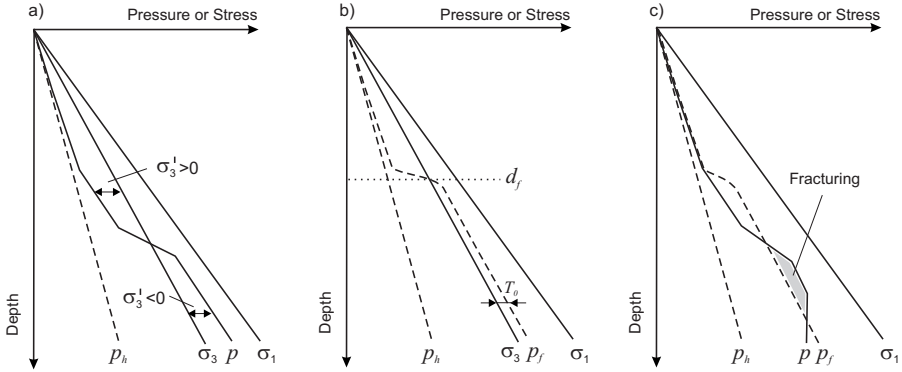


**Fig. 2.45.** Pressure and stress versus depth diagram for a fracturing model with hydrostatic pressure  $p_h$ , pore pressure  $p$ , fracturing pressure  $p_f$ , principal bulk stresses  $\sigma_1$ ,  $\sigma_3$  and effective stresses  $\sigma'_1$ ,  $\sigma'_3$ . The maximum stress is almost equal to the lithostatic pressure and the minimum stress is assumed to be a fixed fraction of the lithostatic pressure. (a) The difference between the minimum and maximum effective stress increases with depth. (b) The Griffith model defines the fracturing pressure as the required pore pressure to initiate fracturing. (c) Fracturing occurs when the pore pressure exceeds the fracturing pressure

$$\log k_f = \log k + \lambda_k \frac{p - p_f}{p_f}, \quad p_c = p_{cf} - \lambda_c \frac{p - p_f}{p_f} \quad (2.86)$$

where  $k$  and  $k_f$  are the permeability of the unfractured and fractured rock,  $p_c$  and  $p_{cf}$  are the capillary entry pressures of the unfractured and fractured rock, and  $\lambda_k$  and  $\lambda_c$  are the fracturing parameters. For clastic rocks, the fracturing parameters of  $\lambda_k = 3 \log \text{mD}$  and  $\lambda_c = 3 \text{ MPa}$  are frequently used. Fractures can partially anneal when the overpressure decreases below the minimum effective stress, so that the tension turns into compression. It is usually not necessary to exceed tensile strength again when fractures are re-opened, that means that the pore pressure has to be equal to the minimum effective stress. In some models, the simplified fracturing condition, that the fracturing pressure is equal to the minimum principal stress, is used. However, the inclusion of multiple closing and opening behaviors requires hysteresis effects with different fracturing pressures and permeabilities.

## 2.7 Faults

Faults occur in most basins with large variations in length, thickness, throws, gouge content and related properties. They play an important role in fluid flow and pressure formation. Faults are initiated in consolidated sediments due to extensional and compressional forces mainly caused by plate tectonics. The process of fault formation and growth can be described and modeled with



kinematic approaches. This is usually not part of basin modeling, instead the fault geometry and main properties at present and paleo-times are given as a predefined input. Geologists distinguish between normal, reverse, transform and strike-slip faults, although most of the faults are mixed mode faults. The fault type depends on stress conditions in the of formation Fig. 2.46. The fault properties can be predicted by structural or fault seal analysis methods.

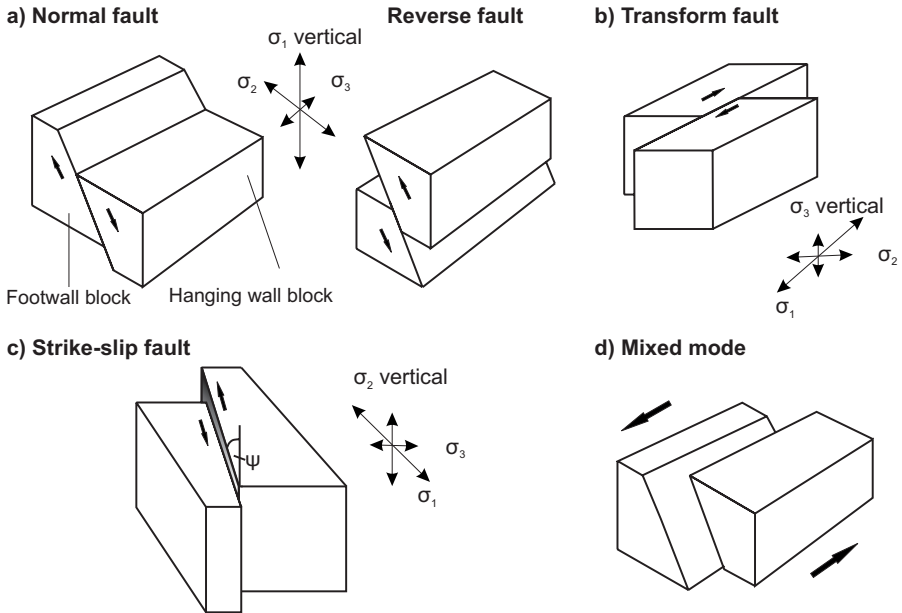


**Fig. 2.46.** Fault types formed under different stress conditions: (a) maximum principal stress in a vertical direction cause normal and reverse faults. (b) Minimum principal stress in a vertical direction causes transform faults. (c) Medium principal stress in a vertical direction causes strike-slip faults. (d) Most faults in nature are mixed modes. The pictures are from Bahlburg and Breitzkreuz (2004)

Fault extensions often exceed several hundreds of meters. Fault zones are often in the range of several meters and much smaller than gridcells of basin scale models. Location and orientation of faults are thus geometrically described with fault planes in 3D-models and lines in 2D-models. Fault lines and planes can be approximated with boundary elements along cell faces and edges in cellular models as illustrated in Fig. 2.47 and Fig. 2.55. The fault planes in 3D-models are constructed from fault lines, which are usually interpreted from seismic at the surface of horizon maps.

Faults can act as preferred migration avenues (in-fault flow) or as hydrocarbon seals which hold column heights of hydrocarbons. The two related flow properties are permeability and capillary entry pressure. Boundary fault

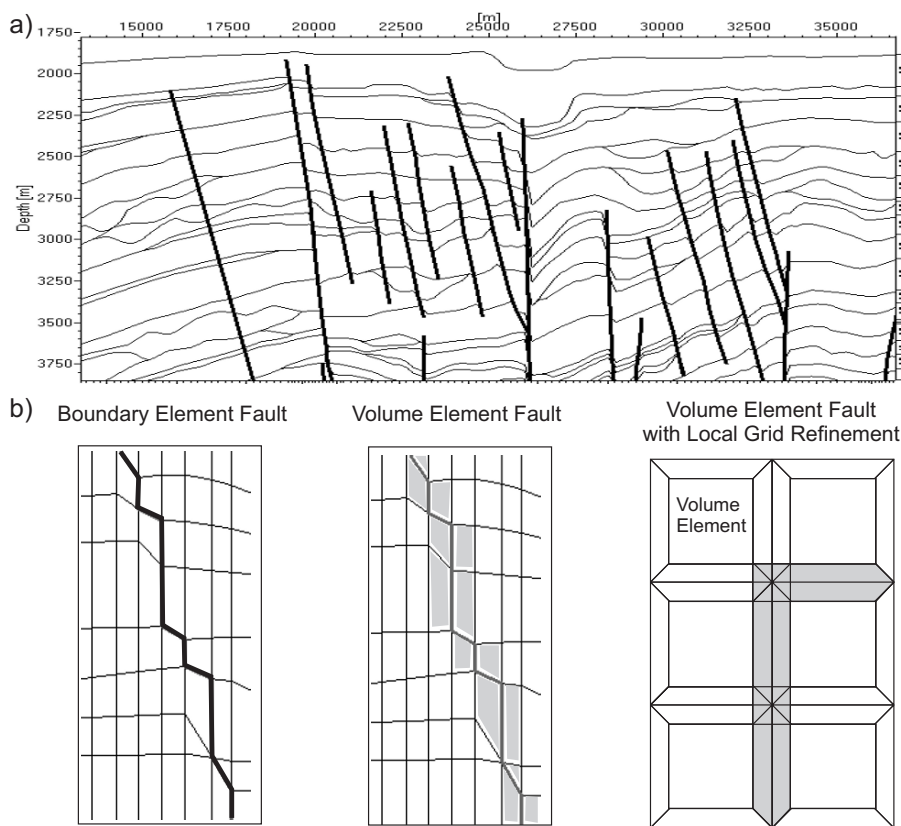


**Fig. 2.47.** 2D-fault models. (a) Fault lines in a 2D-cross section. (b) Fault line approximation with boundary elements, adjacent volume elements, or with locally refined grid cells

elements can be used for modeling petroleum migration and accumulation. They act between two volumetric elements with a zero volume. Capillary entry pressure can be defined for cells with an infinitesimally small volume, but permeabilities cannot be assigned to boundary elements without a volume. This yields instantaneous flow for in-fault flow, which is assumed in some petroleum migration models anyway.

Permeabilities can not be neglected for pore pressure calculations, if fault gouge material with low permeability causes pressure contrasts and compartmentalization. Hence, the inclusion of fault permeabilities for pressure modeling requires the consideration of a fault volume.

The simplest method to work with volumetric fault elements is to define all cells adjacent to the fault plane as fault cells and assign the corresponding fault permeabilities. Obviously, fault zones can be overestimated with this

approach, which can yield large errors in the calculated pressures. This is especially problematic for very low permeability faults, which have to be continuously connected to model compartments. Double or triple bands of cells are necessary when topologically regular grids are considered. Irregular grid-line spacing with higher gridline density in the vicinity of faults can be used to lower the effect, but this is usually only applied in 2D-models, since the number of gridcells increases significantly.

A good solution to the problem is the introduction of locally refined elements around faults (Figs. 2.47, 8.13), where the real fault width can be taken into account. This method requires significant effort for the development of automatic meshers in 3D, especially for the special cases of layer pinch-outs and dendritic fault segments. An example pressure calculation with locally refined elements around faults, fault widths of 10 m and fault permeabilities of  $10^{-6}$  mD is shown in Fig. 2.56. The pressure is constant within the sandstone compartments and varies in the sandy shales.

The fault permeabilities and capillary pressures are mainly determined by the gouge composition. Very thin faults can be handled as neutral or juxtaposition faults without any property assignment.

The gouge composition is a mixture of the rocks of all layers, which slipped along the location during faulting. An important parameter of the composition is the clay content. Various indicators are proposed (Yielding et al., 1997; Fulljames et al., 1996), such as the shale smear factor or the shale gouge ratio (Fig. 2.48). All of them pay attention to the juxtaposition of sediments between the foot and the hanging wall and depend on fault distance or throw. The shale gouge ratio (SGR) is the volumetric ratio of grains smaller than 100 nm to the larger grains assuming that the value at an actual location is simply the arithmetic average of all the material that slipped since fault movement began. In this approach, it is not considered that different rock types have different supply rates to the gouge. An advantage of the SGR concept is, that the values can be calculated by simple volumetrics of the fault adjacent sediments for each point on the fault surface.

Yielding (2002) proposed simple relations to convert SGR values to capillary entry pressures and permeabilities. Capillary entry pressures control column heights at sealing faults. They are given as mercury-air values and can be converted to the present petroleum-water system via in-situ interfacial tension values of the compositional dependent petroleum phases. The fault capillary pressures (FCP) are therefore capillary entry pressures for the mercury-air displacement. Yielding found linearly increasing FCP values for SGR larger than a threshold SGR, with different ascent angles but unique minimum SGR of 18% in most of the samples. The average value for the parameter  $k$  in the following equation is 50 MPa.

$$p_c = k (\text{SGR} - 0.18) . \quad (2.87)$$

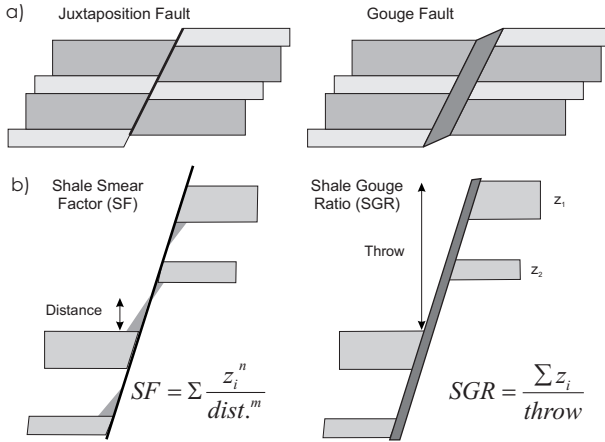


**Fig. 2.48.** Definition of fault properties after Yielding et al. (1997): (a) juxtaposition and gouge fault, (b) definition of shale smear factor (SF) and shale gouge ratio (SGR)

The permeability value controls in-fault flow, once the accumulation is able to break into the fault, but this seems to be less important as the distances are usually short before an exit to more conductive sediments is found.

It is obvious, that the fault properties (SGR, FCP) experience large variations through geological time. Thus, they have to be specified or precalculated for several time periods. A common simplification is the introduction of special fault properties: ideal open (SGR < 18%, FCP < 0.1 MPa) and ideal closed (SGR > 95%, FCP > 50 MPa) to define faults as completely open or completely closed or via special FCPs or SGRs as in Fig. 2.57.

Diagenetic processes or cataclasis in faults can be described by additional temperature or effective stress dependent corrections of the SGR values.

## 2.8 Paleo-Models

In a basin with low faulting, throw and tectonics, back-stripping of the present day geometry under consideration of decompaction, erosion and paleo-thickness corrections is a good approximation of the paleo-geometries. Decompaction and erosion are typically vertical phenomena, which do not take into account any horizontal movements and changes in the total length of the layer. Horizontal movements of single layers like salt domes are described with paleo-thickness corrections based on rock volume balances which results in layer squeezing and stretching. Complex tectonic events often yield strongly deformed geometries, which usually overstretch the possibilities of backstripping. Complete paleo-geometries are alternatively used as input for the simulation. They are constructed from structural modeling methods before basin modeling is performed. The simulator then jumps from predefined

paleo-geometry to paleo-geometry in the analysis. It has to identify the new location of each single facies and has to take into account facies movements and deformations. In compressional tectonics, overthrust layers can multiply be defined along a depth line, which is handled in practice with the implementation of a block concept for the thrust belts. Each block represents a compartment treated as a separate unit which can be moved along and against any other block.

### 2.8.1 Event-Stepping

Backstripping is also called event stepping, since the paleo-geometries are reconstructed from the present day geometry due to given “geological events” with a suitable set of sophisticated rules, which yields topologically similar paleo-models. Decompaction of a layer from present day thickness  $d_p$  to depositional thickness  $d_0$  is calculated with the assumption of the conservation of the solid matrix volume according to

$$d_0 (1 - \phi_0) = d_p (1 - \phi_p) \quad (2.88)$$

with present day and depositional porosities  $\phi_p$  and  $\phi_0$ , respectively. The present day porosity is not known prior to analysis, since it depends on the pore pressure development. Hence, the decompaction in the first simulation run can only be made with an estimation of the present day porosities, used as the steady state values for hydrostatic pressure conditions. The forward simulation then yields calculated present day geometry based on pore pressure controlled compaction, which usually differs from the given present day geometry (Fig. 2.49). This difference is much smaller in the next simulation run, when the calculated present day porosity can be derived for decompaction instead of the estimated steady state values. This optimization procedure can be applied multiple times, but usually two or three loops yield good results.

Modeling of erosion requires the definition of the eroded thicknesses and the erosion ages. Eroded thicknesses can be given with virtual horizons or thicknesses at the time of deposition, at present day or any other geological event (Fig. 2.50). Multiple erosions of one layer and one erosion on multiple layers can also easily be recognized with virtual horizons. The interpretation of eroded thickness is often easier to perform on a backstripped and decompacted paleo-geometry. Herein, the porosity at the erosion age has also to be considered for decompaction of overconsolidated rocks. The eroded thickness and the compaction history of the layer before erosion has to be taken into account in the optimization procedure.

Horizontal movements of layers like salt can be described with additional thickness maps during doming. The changes are realized by layer stretching and thinning. The additional salt thickness layer should be calculated under the assumption of total volume conservation. The simplest model considers a homogeneous depositional layer with the total volume equal to the total

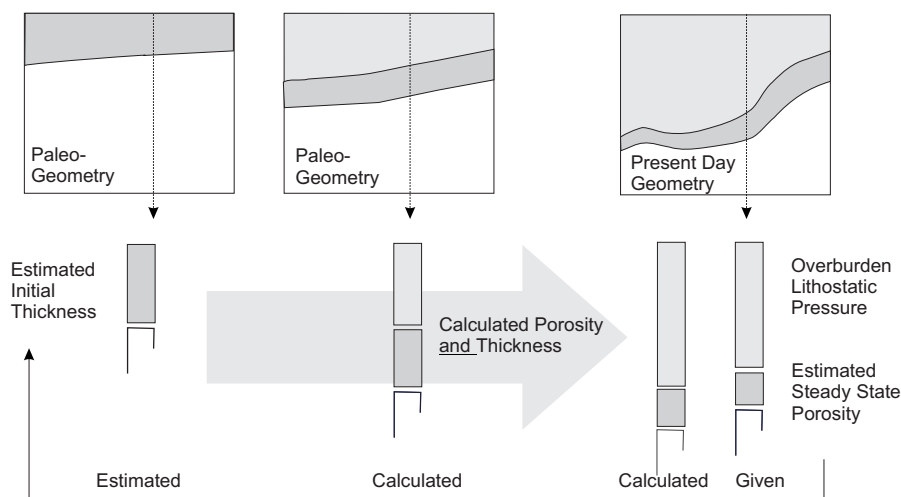


**Fig. 2.49.** Backstripping with decompaction is based on estimated present day porosities. The calculated porosities of the forward simulation usually improve backstripping in the next run

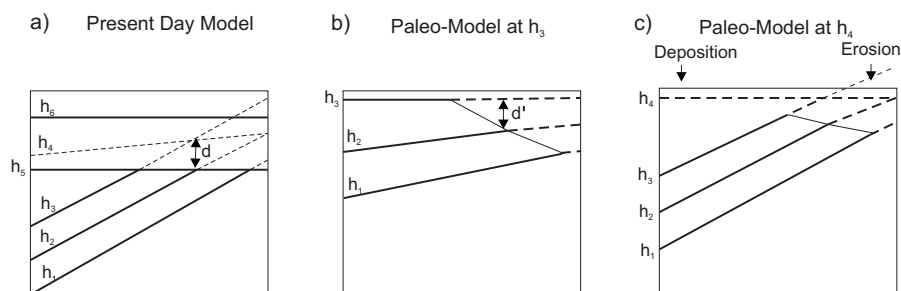


**Fig. 2.50.** Definition of erosional thicknesses: (a) with virtual horizons at the present day geometry, (b) with additional thicknesses at the time of sedimentation, (c) with virtual horizons at any geological event

volume of the present day salt domes and the definition of the doming ages. A linear interpolation between the initial and the final salt thicknesses can then be realized during doming. The opening of the salt windows should be described with an additional salt map, since the salt windows would otherwise open only during the last time step of the doming (Fig. 2.51).

Structural geologists often provide salt maps for various geological events based on kinematic models, which also can be considered during simulation. Additional thickness maps can be used for the thinning of the salt adjacent layers or for doming of other lithologies, e.g. shale. High overburden can also yield reverse domes and single salt pillows as illustrated in Fig. 2.52. This

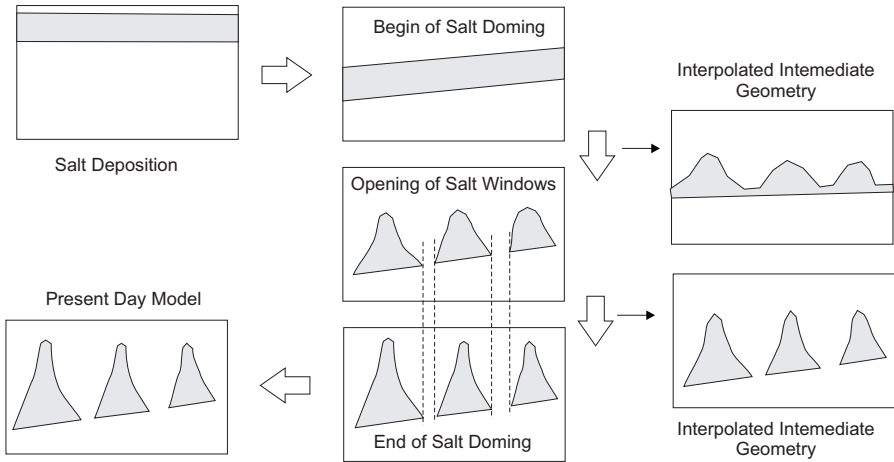


**Fig. 2.51.** A simple geometrical model with a linear interpolation of the salt thicknesses between the geometries of salt sedimentation, salt window opening and the final doming

requires the introduction of several layers to avoid multiple occurrences of one layer along a depth-line. Another method for handling salt intrusions into the overburden layers is to exchange the lithology of the intruded layers with salt. This is recommended when the intruded layers have big gaps in the present geometry. In very complex basins, pre-computed paleo-geometries might be necessary. This is described in the next subsection.

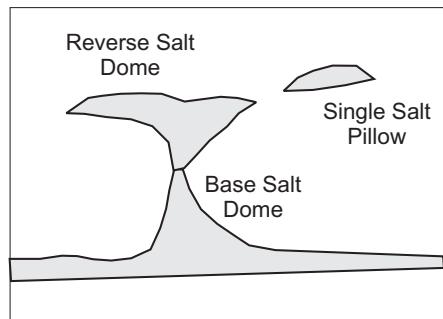


**Fig. 2.52.** Reverse salt domes and salt pillowing require multiple layer definitions

### 2.8.2 Paleo-Stepping

The introduction of complete geometrical models for certain paleo-times requires the recognition of facies locations together with the corresponding types of movements and deformations during stepping from one paleo-geometry

to the next. A section of a layer can be folded, migrated and/or otherwise stretched so that location and shape in two successive time steps might be very different (Fig. 2.53). A meshing algorithm based on pre-defined gridpoints and sublayers can yield new volumetric cells which are no longer related to the same rock of the previous time step. The consequence is that all bulk rock properties have to be transferred according to the new location.

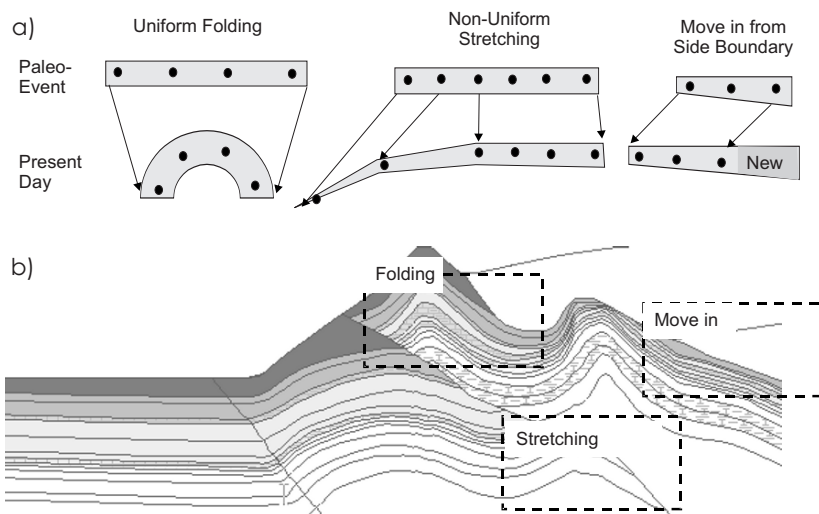


**Fig. 2.53.** Deformation types of facies during tectonics

In most cases, the deformation is uniform stretching or thinning, which can be achieved with linear mapping operations. Any non-uniform deformations have to be specified manually between paleo-geometries. For moving-in layers, the side boundary values can be taken as the values for the previous time step.

In the following a method is described, how the pressure and compaction problem is solved, when the compaction has already been predefined via paleo-geometries. Both the pressure and the compaction equations can be solved in the usual way. The change in the overburden load of each layer is calculated from one paleo-geometry to the next. The transient equation for overpressure (2.13) can then be solved with the transformed cell values of the previous time step. The results are a change in the overpressure as well as a reduction in the porosity. The only difference from the usual procedure is, that the porosity change is not converted into the new layer thicknesses, since they are already predefined with given paleo-geometries. Hence, porosity reduction and compaction are decoupled processes here and it is accepted that the volume rock matrix is no longer conserved.



Backstripping or event-stepping is applied before the first occurrence of a paleo-geometry with the usual method for optimization (Fig. 2.54).

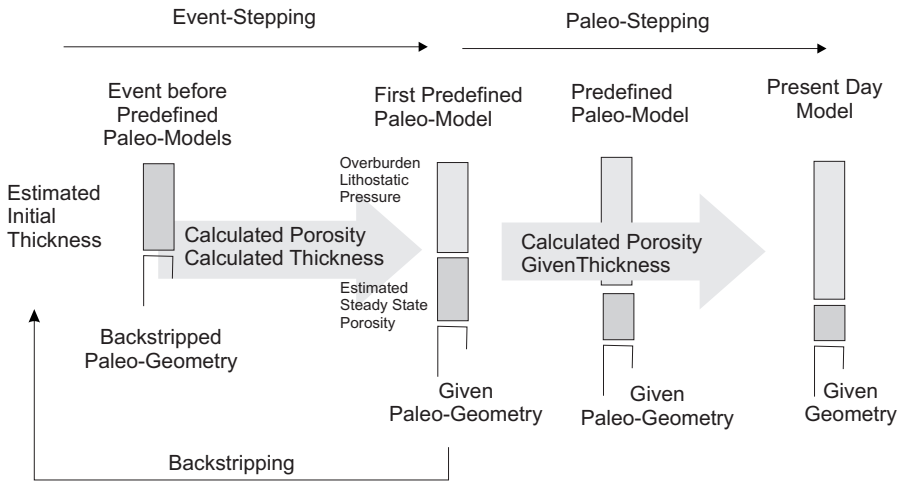


**Fig. 2.54.** Decoupling of compaction and porosity calculation during paleo-stepping

A difficult problem is the automatic generation of additional paleo-models for time steps between the interpretations. The simplest idea is to use linear interpolations so that the thickness values of each gridpoint are interpolated, but this often yields unsuitable connections in steep faults. Another method is to directly jump to the next paleo-model, and use intermediate time steps for the solution heat and fluid flow equations, but with the same geometry for the whole geological event.

The above procedure clearly separates structural reconstruction from forward basin modeling analysis by work flow and by data. The advantage of this decoupled link is that it is possible to use advanced special tools for both structural and basin modeling and the functionality of both tools are retained. Due to decoupling of processes information is lost. Feedback between modeled processes as well as coupled tools, handling structural and basin modeling together, are principally possible.

### 2.8.3 Overthrusting

Blocks for overthrust belts are introduced to avoid multiple layer occurrences along one depth-line (Fig. 2.58). Each block is then treated like a "single basin model" with suitable and varying coupling conditions between the block boundaries. The number of blocks can vary during paleosteps, since the breaking of a so called super block into separate pieces leads to the development of complex block substructures from a homogeneous initial model. A hierarchy

of block heritages has to be specified as a model input. Splitting of a super block into subblocks also has to be taken into account when considering the shift of the fundamental layer values according to their new locations.

All block boundaries are faults. They can be treated as neutral (juxtaposition), partially or ideally open or closed faults with capillary entry pressures and permeabilities (Sec. 2.7).

Compression or extension yields a total section abbreviation or stretching, which yields an increase or decrease in horizontal stress and causes additional or retarded overpressuring and compaction. Then, compaction should be controlled by mean effective stress instead of vertical effective stress components with the following modified compaction law, which replaces equation (2.3).

$$\frac{\partial \phi}{\partial t} = -C_v \frac{\partial \bar{\sigma}'}{\partial t} = -C_v \frac{\partial (\bar{\sigma} - p)}{\partial t} == -C_v \frac{\partial (\bar{\sigma} - p_h - u)}{\partial t} \quad (2.89)$$

where  $C_v$  is the volumetric bulk compressibility, which is related to the Terzaghi compressibility  $C_T$  as follows:<sup>5</sup>

$$C_v = C_T \frac{3(1-\nu)}{1+\nu} \quad (2.90)$$

which yields a factor of 1.28...2.45 for Poisson ratios of  $\nu$  of 0.1...0.4. The pressure equation (2.13) is modified as follows.

$$\frac{C_v}{1-\phi} \frac{\partial u}{\partial t} - \nabla \cdot \frac{\mathbf{k}}{\nu} \cdot \nabla u = \frac{C_v}{1-\phi} \frac{\partial (\bar{\sigma} - p_h)}{\partial t} \quad (2.91)$$

where  $p_h$  is the hydrostatic pressure and  $\bar{\sigma}$  is the mean total stress. Assuming, that the total stress differs from Terzaghi's lithostatic pressure assumption only by an additional horizontal stress component the tectonic stress  $\sigma_t$ , the total mean stress is related with the overburden weight pressure  $p_l$  as follows:

$$\bar{\sigma} = \sigma_v + 2\sigma_h = \frac{1+\nu}{3(1-\nu)} p_l + 2\sigma_t. \quad (2.92)$$

The additional assumption of a uniform compression  $\sigma_t > 0$  or extension  $\sigma_t < 0$  with a constant tectonic stress  $\sigma_t$  yields a simple extension of the pressure equation and compaction law which includes tectonic processes.

<sup>5</sup> In the case without tectonics, it is  $\sigma_h/\sigma_v = \nu/(1-\nu)$  and with  $\bar{\sigma} = (1/3)(\sigma_v + 2\sigma_h)$  it follows that  $\sigma_v/\bar{\sigma} = 3(1-\nu)/(1+\nu)$ .

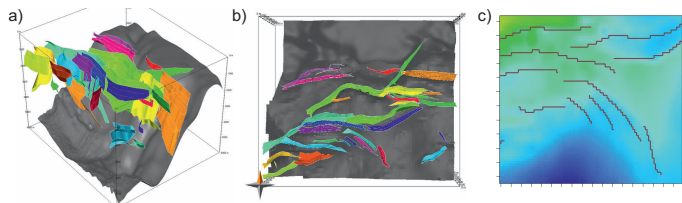


**Fig. 2.55.** (a) Fault approximation with boundary elements in 3D. (b) Vertical view with horizontal fault elements. (c) Map view of cutout with fault traces

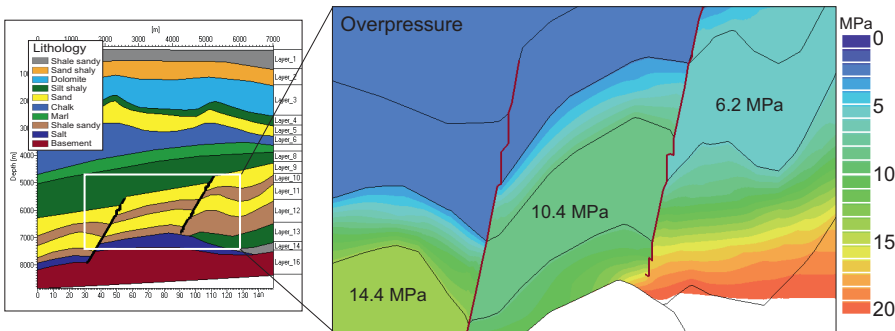


**Fig. 2.56.** Overpressure example with locally refined elements around faults

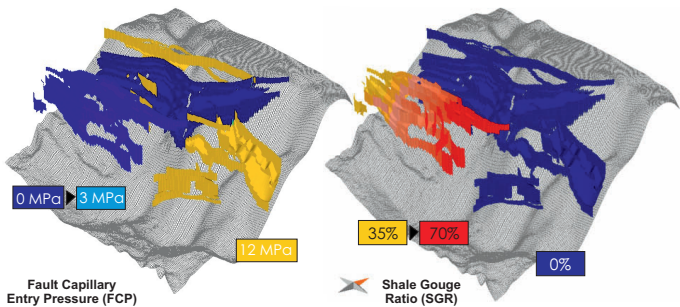


**Fig. 2.57.** Capillary pressures and SGR values on fault planes in a 3D-model

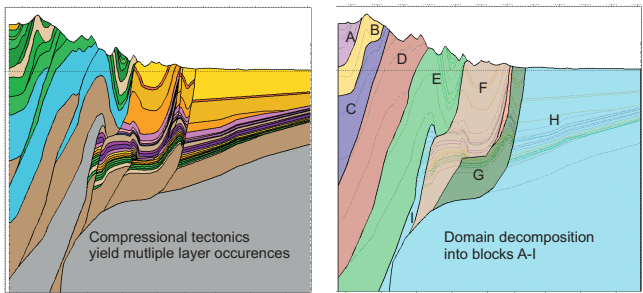


**Fig. 2.58.** Introduction of blocks for compressional tectonics

**Summary:** Overburden load and tectonic stresses cause rock stresses, fluid pressure formation, and sediment compaction. An external load on a bulk volume element is balanced partially by the rock skeleton and partially by the pore water. Rock stresses and pore water pressure equalize overburden and external tectonic stresses.

Many geomechanical processes are formulated with overpressure instead of pore pressure and effective stress instead of total rock stress. Overpressure is pore pressure minus hydrostatic pressure, which is the weight of the overlying pure water column (plus a depth independent shift for zero level adjustment). Effective stress is the total stress minus pore pressure.

Water is mobile. Overpressure gradients causes pore fluid flow, which is mainly controlled by the rock permeabilities. This allows for further rock compaction with reordering of grains. The rock becomes more dense and its internal stress rises as overpressure is usually reduced.

All basic effects of mechanical compaction and overpressure formation can be modeled quite accurately with a Terzaghi-type approach. It is based on the assumptions that rock grains and water are incompressible and that rock compaction is a function of the vertical effective stress only, which is called lithostatic pressure. Water flow is modeled with Darcy's law. Overall mass conservation is taken into account. Appropriate conditions for water in- and outflow at model boundaries must be defined.

Various models for compaction vs. effective stress are proposed. The main characteristic is a logarithmic dependency of effective stress on porosity. The related compaction or bulk compressibilities functions are well known over a wide porosity range for various lithotypes.

Overpressure calibration is a two step process. Firstly, the material parameters of the compaction law must be fitted locally to suitable porosity vs. effective stress relationships. Secondly, permeabilities of relevant layers, which control the overall water flow, must be adjusted. The second step is rather sophisticated and relies on full simulation runs due to possibilities of long range lateral water flows.

Besides pure mechanical compaction, pressure effects due to cementation of pore space, aquathermal expansion, mineral transformations and petroleum generation are found as locally significant.

Alternatively to a calculation of the geometry from compaction laws (event-stepping) the geometry might be imported from purely structural analysis (paleo-stepping). However, overpressures and effective stresses are simulated in any case with similar algorithms.

Faults can be approximated with special volumetric and boundary elements. The main mechanical properties are fault transmissibilities and capillary entry pressures, which can be derived from measured or calculated shale gouge ratios. The inclusion into pressure and fluid flow analysis requires sophisticated numerical models.

## References

- L. F. Athy. Density, porosity and compaction of sedimentary rocks. *American Association of Petroleum Geophysicists Bulletin*, (14):1–24, 1930.
- H. Bahlburg and C Breitzkreuz. *Grundlagen der Geology*. Elsevier GmbH, Muenchen, second edition, 2004.
- M. A. Biot. General theory of three-dimensional consolidation. *Journal of Applied Physics*, (12):155–164, 1941.
- P. A. Bjørkum. How important is pressure in causing dissolution of quartz in sandstones. *Journal of Sedimentary Research*, 66(1):147–154, 1996.
- P. A. Bjørkum and P. H. Nadenau. Temperature Controlled Porosity/Permeability Reduction, Fluid Migration, and Petroleum Exploration in Sedimentary Basins. *APPEA Journal*, 38(Part 1):452–464, 1998.
- P. A. Bjørkum, E. H. Oelkers, P. H. Nadeau, O. Walderhaug, and W. M. Murphy. Porosity Prediction in Quartzose Sandstones as a Function of Time, Temperature, Depth, Stylolite Frequency, and Hydrocarbon Saturation. *AAPG Bulletin*, 82(4):637–648, 1998.
- P. A. Bjørkum, O. Walderhaug, and P. H. Nadeau. Thermally driven porosity reduction: impact on basin subsidence. In *The Petroleum Exploration of Ireland's Offshore Basins*, volume 188 of *Special Publication*, pages 385–392. Geological Society of London, 2001.
- A. Danesh. *PVT and Phase Behaviour of Petroleum Reservoir Fluids*. Number 47 in Developments in petroleum science. Elsevier, 1998.
- P. M. Doyen. Permeability, Conductivity, and Pore Geometry of Sandstone. *Journal of Geophysical Research*, 93(B7):7729–7740, 1988.
- W. A. England, A. S. MacKenzie, D. M. Mann, and T. M. Quigley. The movement and entrapment of petroleum fluids in the subsurface. *Journal of the Geological Society, London*, 144:327–347, 1987.
- E. Fjaer, R. M. Holt, P. Horsrud, A. M. Raan, and Risnes R. *Petroleum related rock mechanics*. Elsevier, 1992.
- J. R. Fulljames, L. J. J. Zijerveld, R. C. M. W. Franssen, G. M. Ingram, and P. D. Richard. Fault seal processes. In Norwegian Petroleum Society, editor, *Hydrocarbon Seals - Importance for Exploration and Production*, page 5. Norwegian Petroleum Society, Oslo, 1996.
- M. R. Giles, L. Indrelid, and D. M. D. James. Compaction – the great unknown in basin modelling. In S. J. Düppenbecker and J. E. Iliffe, editors, *Basin Modelling: Practice and Progress*, number 141 in Special Publication, pages 15–43. Geological Society of London, 1998.
- Hewlett-Packard. Petroleum fluids, manual. Technical Report HP-41C, 1985.
- C. Hilgers, S. Nollet, J. Schönherr, and J. L. Urai. Paleo-overpressure formation and dissipation in reservoir rocks. *OIL GAS European Magazine*, (2): 68–73, 2006.
- R. H. Lander and O. Walderhaug. Predicting Porosity through Simulating Sandstone Compaction and Quartz Cementation. *AAPG Bulletin*, 83(3): 433–449, 1999.

- O. Lauvrak. Personal communication, 2007.
- X. Luo and G. Vasseur. Contributions of compaction and aquathermal pressuring to geopressure and the influence of environmental conditions. *AAPG Bulletin*, 76(10):1550–1559, 1992.
- X. Luo and G. Vasseur. Geopressuring mechanism of organic matter cracking: Numerical modeling. *AAPG Bulletin*, 80(6):856–874, 1996.
- G. Mavko, T. Mukerji, and J. Dvorkin. *The Rock Physics Handbook*. Cambridge University Press, 1998.
- C. I. Mc Dermott, A. L. Randriamantjatosoa, and Kolditz O. Pressure dependent hydraulic flow, heat transport and geo-thermo-mechanical deformation in hydrate crystalline geothermal systems: Preliminary application to identify energy recovery schemes at urach spa. Technical report, Universitaet Tuebingen, Lehrstuhl fuer Angewandte Geologie, 2004.
- W. D. McCain Jr. *The Properties of Petroleum Fluids*. Pennwell Books, second edition, 1990.
- M. J. Osborne and R. E. Swarbrick. Mechanisms for generating overpressure in sedimentary basins: A re-evaluation. *AAPG Bulletin*, 81:1023–1041, 1997.
- R. H. G. Parry. *Mohr Circles, Stresspaths and Geotechnics*. Spon Press, second edition, 2004.
- A. M. Pytte and R. C. Reynolds. The thermal transformation of smectite to illite. In N. D. Naeser and T. H. McCulloh, editors, *Thermal History of Sedimentary Basins: Methods and Case Histories*, pages 133–140. Springer-Verlag, 1989.
- F. Schneider and S. Hay. Compaction model for quartzose sandstones application to the Garn Formation, Haltenbanken, Mid-Norwegian Continental Shelf. *Marine and Petroleum Geology*, 18:833–848, 2001.
- F. Schneider, J. L. Potdevin, S. Wolf, and I. Faille. Mechanical and chemical compaction model for sedimentary basin simulators. *Tectonophysics*, 263:307–313, 1996.
- D. Schulze-Makuch, D. S. Carlson, D. S. Cherkauer, and Malik P. Scale dependency of hydraulic conductivity in heterogeneous media. *Groundwater*, 37:904–919, 1999.
- J. E. Smith. The dynamics of shale compaction and evolution of pore fluid pressure. *Mathematical Geology*, (3):239–263, 1971.
- R. E. Swarbrick, M. J. Osborne, and Gareth S. Yardley. Comparison of Overpressure Magnitude Resulting from the Main Generating Mechanisms. In A. R. Huffmann and G. L. Bowers, editors, *Pressure regimes in sedimentary basins and their prediction*, volume 76, pages 1–12. AAPG Memoir, 2002.
- K. Terzaghi. Die Berechnung der Durchlässigkeitsziffer des Tonen im Verlauf der hydrodynamischen Spannungserscheinungen. *Szber Akademie Wissenschaft Vienna, Math-naturwissenschaft Klasse IIa*, (132):125–138, 1923.
- P. Ungerer, J. Burrus, B. Doligez, P. Y. Chenet, and F. Bessis. Basin evaluation by integrated two-dimensional modeling of heat transfer, fluid flow, hydrocarbon generation and migration. *AAPG Bulletin*, 74:309–335, 1990.

- L. Vidal-Beaudet and S. Charpentier. Percolation theory and hydrodynamics of soil-peat mixtures. *Soil Sci. Soc. AM. J.*, 64:827–835, 2000.
- O. Walderhaug. Modeling quartz cementation and porosity in middle jurassic brent group sandstones of the Kvitenbjørn field, northern North Sea. *AAPG Bulletin*, 84:1325–1339, 2000.
- O. Walderhaug. Kinetic modelling of quartz cementation and porosity loss in deeply buried sandstone reservoirs. *AAPG Bulletin*, 5:80, 1996.
- O. Walderhaug, P. A. Bjørkum, P. H. Nadeau, and O. Langnes. Quantitative modelling of basin subsidence caused by temperature-driven silica dissolution and reprecipitation. *Petroleum Geoscience*, 7:107–113, 2001.
- A. Y. Yang and A. C. Aplin. Definition and practical application of mudstone porosity-effective stress relationships. *Petroleum Geoscience*, 10:153–162, 2004.
- G. Yielding. Shale Gouge Ratio – calibration by geohistory. In A. G. Koestler and R. Hunsdale, editors, *Hydrocarbon Seal Quantification*, number 11 in NPF Special Publication, pages 1–15. Elsevier Science B.V., Amsterdam, 2002.
- G. Yielding, B. Freeman, and D. T. Needham. Quantitative Fault Seal Prediction. *AAPG Bulletin*, 81(6):897–917, 1997.
- O. C. Zienkiewicz. *Method of the finite elements*. Carl Hanser, second edition, 1984.



<http://www.springer.com/978-3-540-72317-2>

Fundamentals of Basin and Petroleum Systems  
Modeling

Hantschel, Th.; Kauerauf, A.I.

2009, XVI, 476 p., Hardcover

ISBN: 978-3-540-72317-2